Nuclear Resonance Vibrational Spectroscopy

Chapter · June 2020

DOI: 10.1515/9783110496574-009

3 authors:

Leland Bruce Gee
Stanford University
30 PUBLICATIONS **343** CITATIONS
SEE PROFILE

Hongxin Wang
SETI Institute
119 PUBLICATIONS **2,349** CITATIONS
SEE PROFILE

Stephen Cramer
University of California, Davis
206 PUBLICATIONS **6,359** CITATIONS
SEE PROFILE

Leland B. Gee, Hongxin Wang and Stephen P. Cramer

9 Nuclear resonance vibrational spectroscopy

9.1 Introduction

9.1.1 Mössbauer effect

In a Mössbauer experiment, the intensity directly scales with f_{LM}, such that the observed cross section, σ_N, is reduced from the total cross section according to $\sigma(0) \sim(\pi/2)\, \sigma_N\, f_{LM}$ [6]. However, there is a "sum rule" that states that the integrated cross section for a nuclear transition remains constant [7]. So, where does this missing intensity go? The missing intensity is in the "recoil fraction," $1 - f_{LM}$, where nuclear transitions couple to atomic vibrations, resulting in the creation or annihilation of phonons analogous to Stokes and anti-Stokes features in optical spectroscopies (Figure 9.1). It turns out that this fraction contains useful and detailed information about the vibrational properties of a sample.

Before the advent of modern synchrotron radiation (SR) sources, most experiments probed the recoil fraction indirectly, by observing the loss of Mössbauer intensity [8, 9]. Since the inception of high brightness third-generation synchrotron X-ray sources and high-resolution monochromators (HRMs), we can probe the recoil fraction directly by the technique known as *nuclear resonance vibrational spectroscopy* (NRVS). Other less common names for the technique include nuclear resonant inelastic X-ray spectroscopy, nuclear inelastic scattering (NIS) and the phonon-assisted Mössbauer effect (PAME).

NRVS has applications to chemistry, biology, geology, materials science and physics. It is an exciting tool because:

- NRVS yields a vibrational spectrum for a specific isotope of a specific element,
- the resulting vibrational spectrum is easily calculated and interpreted,
- the isotopic sensitivity allows labeling experiments, say of surfaces or of specific sites in metalloenzymes and
- NRVS also provides quantities such as the speed of sound and average kinetic energy.

Before we continue further, we present a pair of examples as an initial demonstration (Figure 9.1 and Figure 9.2). At one extreme is the spectrum of Fe metal, in which the

Leland B. Gee, Department of Chemistry, Stanford University, California, USA
Hongxin Wang, Stephen P. Cramer, Department of Chemistry, University of California, California, USA

https://doi.org/10.1515/9783110496574-009

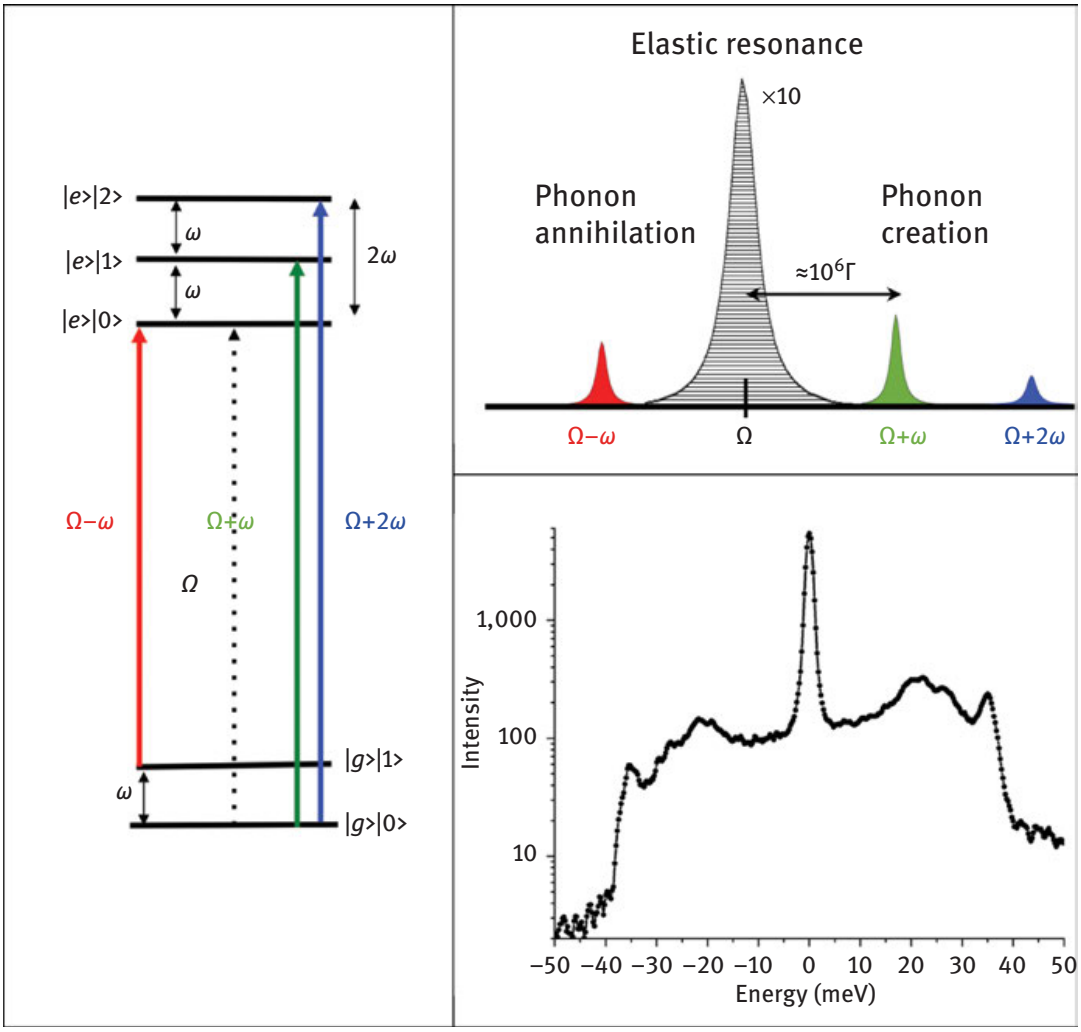

Figure 9.1: Left: State schematic of zero phonon and recoil events for a system with a single fundamental vibrational frequency. The recoil-free Mössbauer line is the |*g*>0> → |*e*>0> transition. Upper right: Comparison of energies and intensities for the same system. The phonon creation or "Stokes" region is to higher energy, with single-phonon and multiple-phonon events. The phonon annihilation or "anti-Stokes" region is at lower energy and has its intensity reduced by the Boltzmann factor (see text). Lower right: NRVS spectrum for Fe metal, typical for a system with a continuous density of states.

vibrations are described as propagating phonons with a continuous density of states. Analysis of such spectra can provide important geophysical properties such as the velocity of sound, specific heat and average vibrational force constant. At the other extreme is the spectrum of $^{57}Fe(S_2C_2H_4)(CO)_2(PMe_3)_2$, an Fe coordination complex with terminal CO ligands. The isolated optical modes from 500 to 650 cm^{-1} are dominantly Fe–CO stretching and bending in character [10].

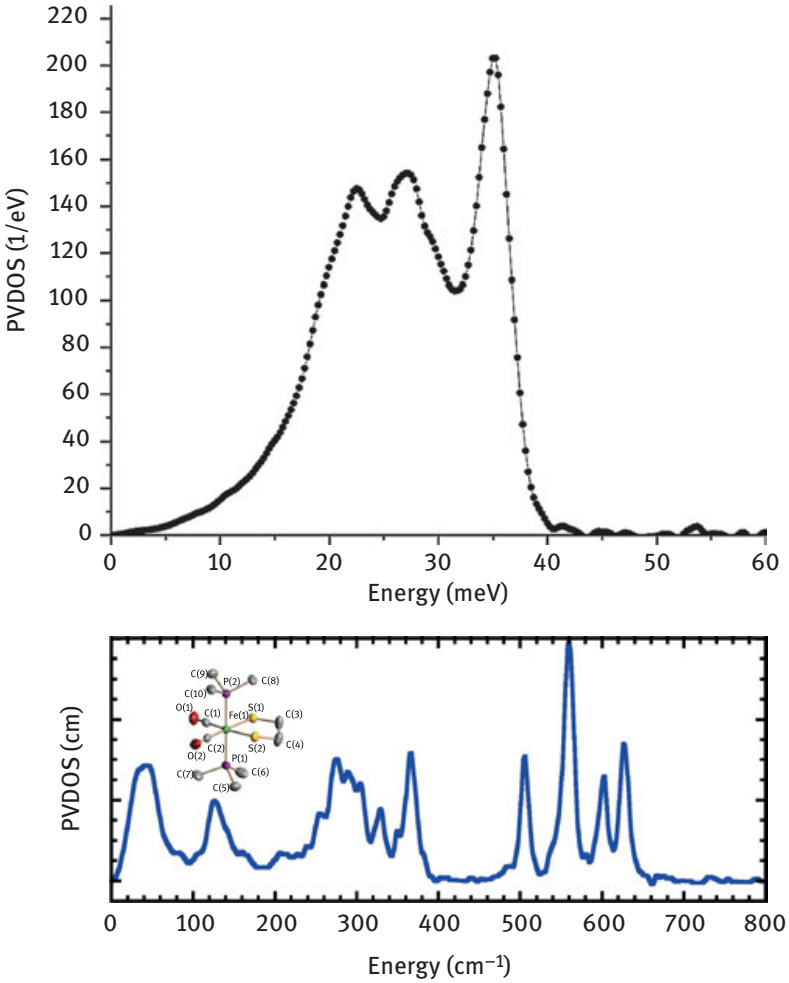

Figure 9.2: NRVS examples. top: The NRVS spectrum for ^{57}Fe Metal. bottom: Spectrum for a complex with two terminal –C≡O ligands [10].

9.1.2 History

NRVS is related to, and descended from, Mössbauer spectroscopy, which focuses on the recoil-free Mössbauer nuclear excitation to learn about the electronic structure of the atom – a recoilless excitation [1, 2, 11]. Probing vibrational dynamics through coupled nuclear transitions was explored in the early 1960s [4, 12]. Typically for Mössbauer spectroscopy, energies incident to the sample are scanned by Doppler shifting a decaying parent isotope. However, the resonances in Mössbauer spectroscopy are usually shifted on the order of neV relative to the nuclear excitation, but vibrational quanta are on the order of meV. This implies a Doppler shifted source would need to move with a velocity 6 orders of magnitude faster than a typical Mössbauer experiment to resolve vibrational modes. Although there were heroic experiments

involving sources mounted onto ultracentrifuges [8, 9], such a Mössbauer spectroscopy setup converted for NRVS is considered impractical and a different type of source is required for NRVS.

The possibility of using a synchrotron as a source for nuclear resonance spectroscopies was first proposed by Ruby in 1974 [13]. The proposition was explored in the mid-1980s by Gerdau [14]. By the mid-1990s with most of the theoretical and practical groundwork laid, three teams near-simultaneously made observations of NIS caused by vibrational dynamics [15–17]. The three teams were based out of the SPring-8, APS and ESRF synchrotrons, and these remain global hubs for nuclear resonance spectroscopies to this day.

After the initial observations, there has been a boom in NRVS research. Due to its ubiquity in chemistry, materials science, biology as well as nuclear properties that are amenable to the timescale of a synchrotron, ^{57}Fe has enjoyed a particular emphasis in NRVS research. One of the first demonstrations of the efficacy of the ^{57}Fe NRVS experiment for dilute biological samples was performed on myoglobin [18, 19]. Since then many bioinorganic ^{57}Fe NRVS experiments have been performed on (not comprehensively) the NiFe site in [NiFe] hydrogenase [20–22], the diiron site in [FeFe] hydrogenase [23, 24], the P [8Fe7S]- and M [7Fe9SMo]- clusters of Mo-nitrogenase [25–28], heme systems [29, 30], nonheme systems [31, 32] and nitric-oxide sensing [4Fe4S] clusters [33]. The rate at which NRVS is answering questions about biological Fe metallocofactors shows no indication of slowing down.

9.2 NRVS intensities for discrete normal modes

How are vibrations and phonons with energies of meV coupled to nuclear transitions at the tens of keV level? The occurrence of vibrational side-bands is one way to understand the NRVS effect. A nucleus vibrating at frequency ω and illuminated by a monochromatic beam at $\omega+\Omega$ will experience a negative side-band at $(\omega+\Omega)-\omega = \Omega$ and hence be in resonance for a nuclear transition. Additionally, a nucleus that is part of a vibrational excited state will be in resonance *via* the positive side-band: $(\Omega - \omega)+\omega = \Omega$.

The overall cross section $\sigma(E)$ for nuclear resonant absorption of a photon with energy E can be factored into two terms, one of which depends on the properties of the nucleus: cross section $\sigma(E_0)$ and lifetime broadening by linewidth, Γ_0:

$$\sigma(E) = \frac{\pi}{2}\sigma(E_0)\Gamma_0 S(E - E_0) \tag{9.1}$$

where the second term, $S(E - E_0)$ is the nuclear excitation probability, which depends on the environment of the nucleus. If one assumes a harmonic lattice or molecule:

$$S(E) = f_{\mathrm{LM}} \left(\underbrace{\delta_{\Gamma}(E)}_{\text{Mössbauer}} + \underbrace{\sum_{n=1}^{\infty} S_n(E)}_{\text{NRVS}} \right) \tag{9.2}$$

where δΓ(E) is a Lorentzian of width Γ and the function $S_n(E)$ refers to events involving n phonons and f_{LM} is the Lamb–Mössbauer factor.

9.2.1 Stokes fundamentals

Suppose that we have a harmonic oscillator molecular system with a set of normal modes labeled α that are described by the displacements $\vec{r}_{k\alpha}$ for atom k and normal mode α. We assume a lineshape function L to account for the experimental resolution and lifetime broadening, and we convert the energy scale for our normal mode α to a frequency $\bar{\nu}_{\alpha}$ in wavenumbers (cm^{-1}). As a specific example, we use the $FeCl_4^-$ ion, which in T_d symmetry will have nine normal modes distributed into four bands. Accounting for degeneracy, the particular modes are labeled ν_1 – corresponding to the totally symmetric (A_1) stretch, ν_2 – corresponding to the doubly degenerate (E) bend, ν_3 – corresponding to the triply degenerate (T_2) stretch and ν_4 – corresponding to the triply degenerate (T_2) bend (Figure 9.3).

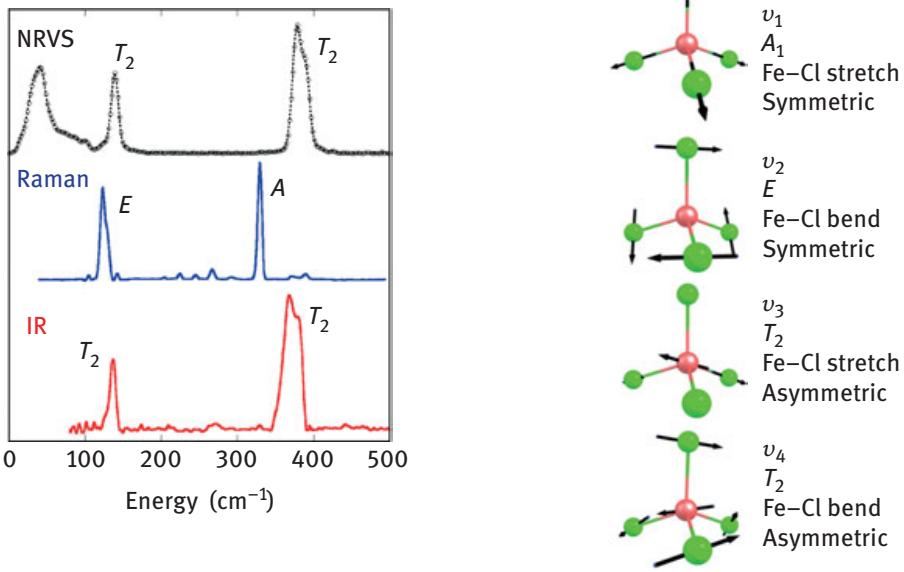

Figure 9.3: NRVS spectra for $(NEt_4)(FeCl_4)$. Left: Comparison of ^{57}Fe PVDOS with Raman and IR spectra, illustrating the dependence of mode strength on the amount of Fe motion. Right: Descriptions of atomic motion in different vibrational modes.

Combining the above, the normalized excitation probability for such a system can then be rewritten as follows:

$$S(\bar{\nu}) = f_{\mathrm{LM}}\mathcal{L}_0(\bar{\nu}) + \sum_{\Delta n_\alpha} \phi(\Delta n_\alpha)\mathcal{L}(\bar{\nu} - \sum_{\alpha} \Delta n_\alpha \bar{\nu}_\alpha) \tag{9.3}$$

In the above expression, $\phi(\Delta n_\alpha)$ refers to the fractional area (integrated probability) corresponding to a transition from initial population n_α to final population $n_\alpha+\Delta n_\alpha$. In the particular case of the $FeCl_4^-$ ion, α would range from 1→4, with appropriate normalization factors to account for the degeneracies.

The NRVS effect depends on the amount of active isotope nuclear motion in a particular normal mode or phonon. The critical term that captures this is the "mode composition factor," $e^2_{j\alpha}$, which is the fraction of kinetic energy associated with motion of nucleus j with mass m_j and mean square displacements $r^2_{j\alpha}$:

$$e^2_{j\alpha} = \frac{m_j r^2_{j\alpha}}{\sum_k m_k r^2_{k\alpha}} \tag{9.4}$$

Then for a randomly oriented sample, and a nuclear transition with recoil energy $\bar{\nu}_R$ and Lamb–Mössbauer factor f_{LM}, an expression that captures the properties that govern NRVS intensity for a fundamental transition from $n_\alpha \rightarrow n_\alpha + 1$ is:

$$\phi_\alpha = \frac{1}{3}\left(\frac{\nu_R}{\nu_\alpha}\right)(\bar{n}_\alpha + 1) f_{\mathrm{LM}} e^2_{j\alpha} \tag{9.5}$$

The term $\bar{n}_\alpha$ is the mean occupation number for mode α and is given by Boltzmann statistics as follows:

$$\bar{n}_\alpha = \frac{1}{\exp\left(\frac{hc\bar{\nu}_\alpha}{k_B T}\right) - 1} \tag{9.6}$$

The mode composition factor is the key term for describing the NRVS intensity of a given normal mode. It thus plays a role similar to the transition dipole moment in IR spectroscopy or the polarizability tensor in Raman spectroscopy. Due to the simplicity of the intensity mechanism, once a normal mode description is obtained from a DFT or empirical forcefield model, it is facile to calculate the normal mode composition factor for the probe atom. In contrast, IR or Raman calculations involve assumptions about molecular properties such as dipole moments or polarizabilities.

In summary, there are four terms that govern NRVS intensities:

- the Lamb–Mössbauer factor,
- a general $1/E$ dependence that reduces intensity of higher energy transitions,
- the temperature, which governs the distribution of occupied ground vibrational levels and
- most important, the mode composition factor.

Because the NRVS signal depends on motion of the nucleus of interest, some modes will be strictly forbidden by symmetry. An example is the totally symmetric stretch of a tetrahedral complex such as $FeCl_4^-$ (Figure 9.3). Modes involving light atom ligands, such as Fe–H stretches, are more difficult to observe because the light atom dominates the motion of the vibrational mode. Higher-frequency modes also suffer from the $1/E$ dependence. As will be discussed later, weak modes can be salvaged to some extent by preferentially weighting the acquisition time as done with region of interest (ROI) scans.

9.2.2 Anti-Stokes intensity

As with Raman spectroscopy, at photon energies $E_0 - \bar{\nu}_\alpha$, there are transitions involving "annihilation" of phonons. The contribution of these "anti-Stokes features' is given by:

$$\phi_\alpha = \frac{1}{3}\left(\frac{\bar{\nu}_R}{\bar{\nu}_\alpha}\right)\bar{n}_\alpha f_{LM} e_{j\alpha}^2 \tag{9.7}$$

In these transitions, $n_\alpha + 1 \rightarrow n_\alpha$, and the intensity is strongly temperature dependent because these transitions start from vibrational excited states. As observed in Figure 9.1 the relative strength of Stokes and anti-Stokes features depends on the temperature via the Boltzmann factor:

$$\frac{\phi_{\text{anti-Stokes}}}{\phi_{\text{Stokes}}} = \frac{\bar{n}_\alpha}{\bar{n}_\alpha + 1} = \exp\left(-\frac{hc\nu_\alpha}{k_B T}\right) \tag{9.8}$$

By rearranging this equation for T, the relative strengths of the anti-Stokes and Stokes transitions at frequencies $\pm\,\bar{\nu}_\alpha$ can be used to determine the sample temperature.

9.2.3 Multiphonon events – overtone and combination bands

Again like Raman and IR spectroscopy, an NRVS spectrum also exhibits overtone bands and combination bands involving changes of two or more phonons. How significant are they? It all depends on the Lamb–Mössbauer factor. By integrating the individual $S_n(E)$ curves, the n-phonon probabilities are obtained:

$$P_n = \int S_n(E)dE = f_{LM}\frac{(-\ln f_{LM})^n}{n!} \tag{9.9}$$

From this, Sturhahn gives a very simple expression for the average number of phonons excited over the nuclear excitation spectrum [34]:

$$\langle n \rangle = -\ln f_{\mathrm{LM}} \tag{9.10}$$

As shown in Figure 9.4, this means that multiphonon contributions are less than 10% of the single phonon contribution as long as $f_{\mathrm{LM}} > 0.83$.

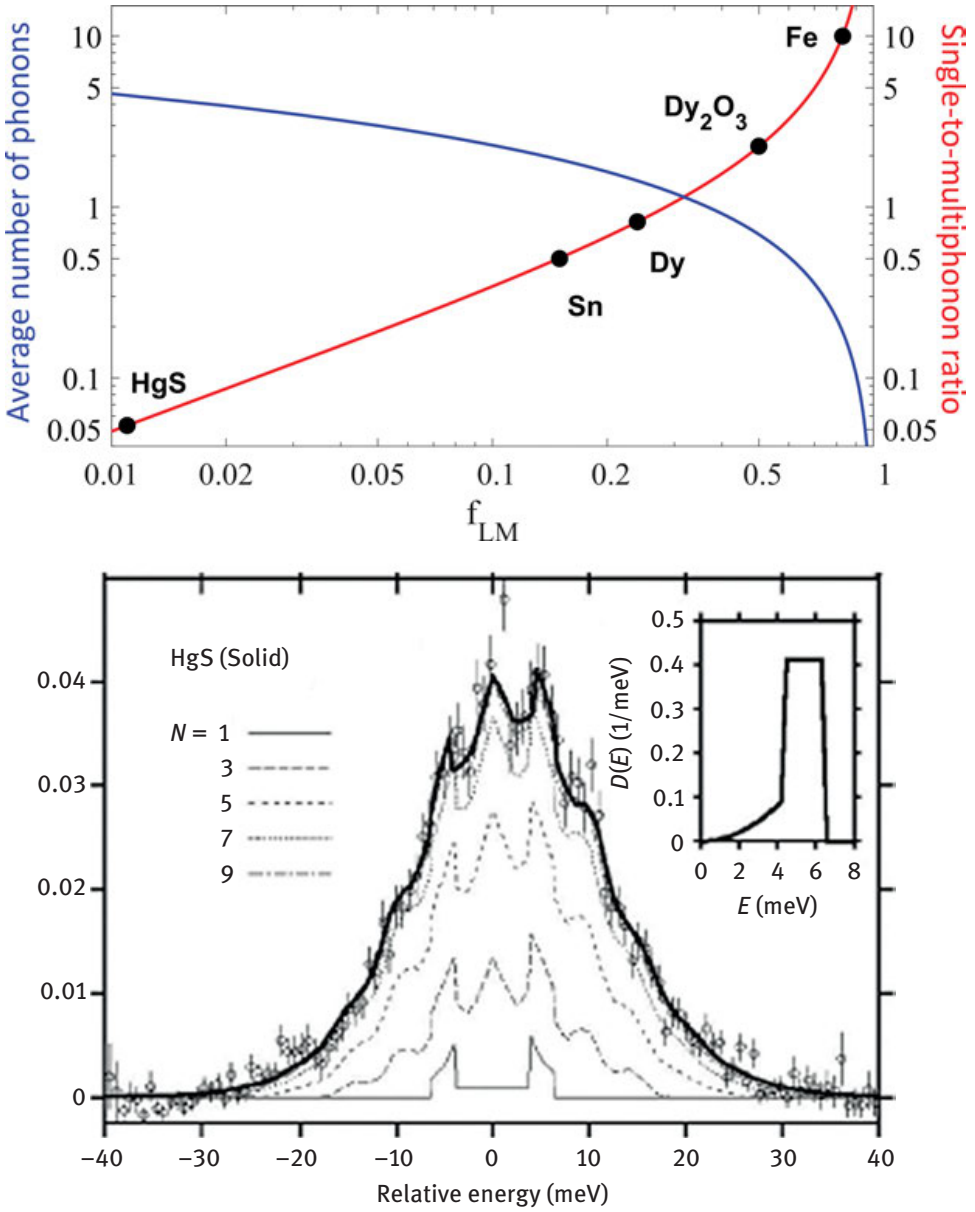

Figure 9.4: Top: The average number of phonons <*n*> (——) (integrated over all transition probabilities) and the ratio of single phonon to multiphonon events (——) as a function of typical elemental Lamb–Mössbauer factors f_{LM}, illustrated for a variety of typical samples and conditions: ^{161}Dy/$^{161}Dy_2O_3$ at 300K [35], ^{201}HgS at 300K [36], β-^{119}Sn at 100K [37, 38], α-^{57}Fe at 300K [39]. Bottom: NRVS spectrum for HgS, an extreme case of multiphonon events (*N*>1) dominating the nuclear spectrum [36].

Sage and coworkers have investigated the properties of two phonon contributions in some detail [40, 41]. In the same low-temperature (high-frequency) approximation used for the single-phonon approximation, the contribution $\phi_{\alpha\alpha}$ of the overtone transition, $n_\alpha \rightarrow n_\alpha+2$, at energy $2\bar{\nu}_\alpha$ is given by eq. (9.11) [41]:

$$\phi_{\alpha\alpha} = \frac{1}{10}\left(\frac{\bar{\nu}_R}{\bar{\nu}_\alpha}\right)^2 e_{j\alpha}^4(\bar{n}_\alpha+1)^2 f_{\mathrm{LM}} = \frac{9}{10}\frac{\phi_\alpha^2}{f_{\mathrm{LM}}} \tag{9.11}$$

We can then take the ratio of eqs. (9.11) and (9.5) to determine the fraction of overtone intensity to single phonon contribution. Assuming an arbitrary value of $\phi_\alpha = 0.02$ and a favorable f_{LM}=0.85, we find that the overtone to fundamental ratio, $\frac{\phi_{\alpha\alpha}}{\phi_\alpha} \approx 2.1\%$. With the same approximations, similar expressions can be derived for the strength $\phi_{\alpha\beta}$ of the combination band, $n_\alpha \rightarrow n_\alpha+1$, $n_\beta \rightarrow n_\beta+1$, at energy $\bar{\nu}_\alpha + \bar{\nu}_\beta$; however in that case, the directions of the two different normal mode motions must also be taken into account [41].

9.2.4 Orientation dependence

Although most NRVS experiments are conducted on powder or solution samples, there is extra information to be gained when oriented or single-crystal samples are available. In the most general case, the NRVS will be different for an incident beam along three perpendicular directions in the sample, *x*, *y* and *z*. There will then be three distinct mode composition factors, corresponding to the projection of the nuclear motion along the three axes.

$$e_{j\alpha,x}^2 = \frac{m_j(r\cdot\hat{x})_{j\alpha}^2}{\sum_k m_k r_{k\alpha}^2}, e_{j\alpha,y}^2 = \frac{m_j(r\cdot\hat{y})_{j\alpha}^2}{\sum_k m_k r_{k\alpha}^2}, e_{j\alpha,z}^2 = \frac{m_j(r\cdot\hat{z})_{j\alpha}^2}{\sum_k m_k r_{k\alpha}^2} \tag{9.12}$$

As illustrated in Figure 9.5, for a crystal with isotope I and neighbor J, the intensity of the I–J stretching mode in the NRVS will vary as $\cos^2\theta$, where θ is the angle between the photon direction and the interatomic axis. This contrasts with the

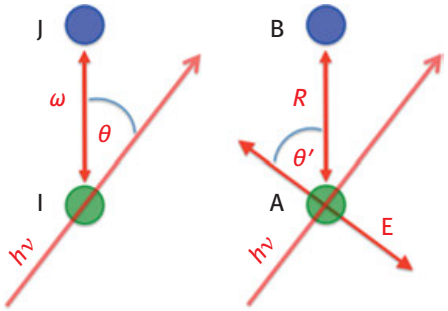

Figure 9.5: Comparison of orientation dependence for NRVS intensity of a stretching mode oriented between atoms I and J and EXAFS intensity from atom A and neighboring atom B.

$\cos^2\theta'$ angular dependence of extended X-ray absorption fine structure (EXAFS), where the θ' refers to the angle between the electric field E vector and the interatomic axis.

In one example of using this orientation dependence, the NRVS for a single crystal of FeOEP(NO) was examined, with the photon beam oriented in three orthogonal crystal axes. The observed intensities were then used to deduce the direction of Fe motion in particular normal modes, such as the Fe–NO bending motions (Figure 9.6) [42].

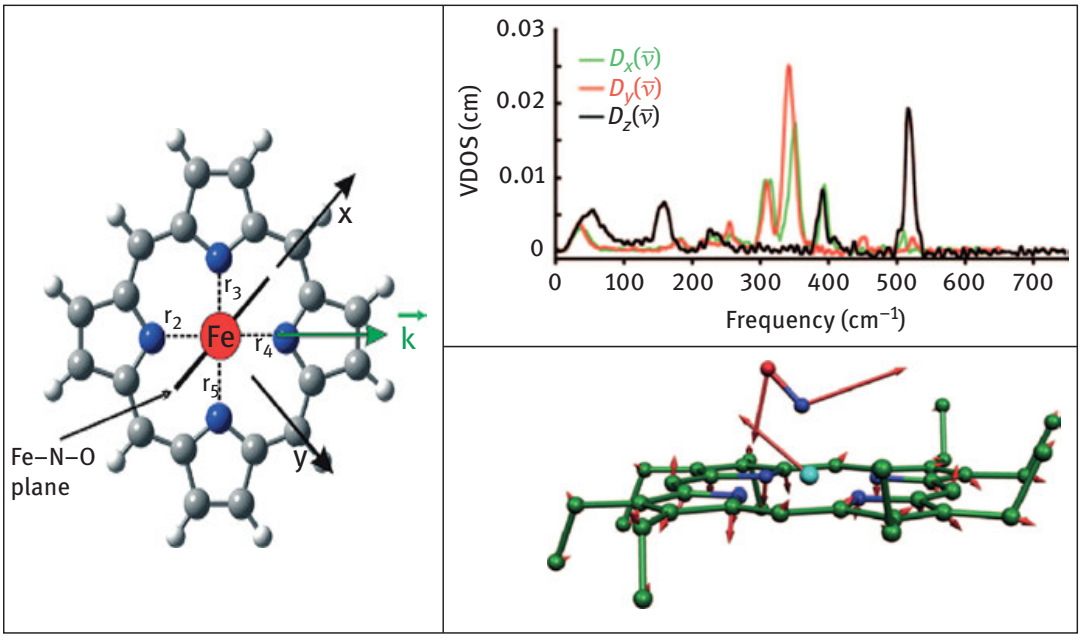

Figure 9.6: Left: Coordinate system used for NRVS on a single crystal of Fe(OEP)NO. Top right: Observed variation. Bottom right: Deduced motion for the Fe–NO bending mode.

9.2.5 Partial vibrational density of states (PVDOS) treatment

The discrete, isolated NRVS features seen in the $(NEt_4)(FeCl_4)$ spectrum are atypical. In most cases, there are many unresolved modes. In fact, apart from localized optical modes, samples will also have delocalized "acoustic" modes that involve motion of the entire unit cell and form a low-energy continuum. For $(NEt_4)(FeCl_4)$ such modes are seen below 80 cm^{-1} (Figure 9.3). For many chemical and biological applications, the low-energy modes are not of keen interest. However, the low-energy modes contain information about properties such as the speed of sound in a sample [43] that are of critical interest to geophysicists. We thus need a way to describe the NRVS for the more general case where the there is a continuous distribution of phonon energies.

These are best described by a continuous "partial vibrational density of states" or PVDOS, commonly written as $D(E)$ or $g(E)$ in the NRVS literature, and $D(E,\hat{k})$ or $g(E,\hat{k})$ if the directional dependence of the PVDOS is retained. This weighted vibrational density of states can be written in terms of photon wavevector $\hat{k}$ and mass weighted normal mode composition factors $\hat{e}_{j\alpha}$ as follows:

$$D_j\left(E,\hat{k}\right) = \sum_j \left(\hat{k}\cdot\hat{e}_{j\alpha}\right)^2 \mathcal{L}(E-E_\alpha) \tag{9.13}$$

From the equation we infer that the experimental density of states will give us a direct description of the mass-weighted normal mode composition factors. Then our goal is to derive the PVDOS from our experimental data.

In the experimental data, there will be differences in penetration depth for the elastic peak, where there is a large absorption cross section, compared to the inelastic region by the incident beam. This complicates determination of the spectral normalization factor (A) as now there is a penetration suppression factor, C, caused by saturation at the elastic peak such that the measured intensity is:

$$I(E) = A\{S(E) - C\delta(E)\} \tag{9.14}$$

Here, we take advantage of Lipkin's sum rule [44] and recognize that the first moment of the spectrum depends only on the recoil energy of the nuclear isotope thus we obtain:

$$\int ES(E)dE = AE_r \tag{9.15}$$

Using eqs. (9.14 and 9.15) together and knowing the zeroth moment of the spectrum should be unity we can calculate the penetration suppression factor:

$$C = 1 - \frac{1}{A}\int I(E)dE \tag{9.16}$$

Next, we can further interpret the spectrum by approximating the interatomic potential V as quadratic with respect to interatomic displacements (the harmonic approximation). The total excitation probability becomes similar to eq. (9.2):

$$S(s,E) = f(s)\delta(E) + \sum S_n(s,E) \tag{9.17}$$

where S_n is the excitation probability of a phonon of order n. For the harmonic approximation, the single-phonon contribution to the probability is:

$$S_1(s,E) = \frac{E_R}{E(1-e^{-\beta E})}g(s,|E|) \tag{9.18}$$

Where $g(s,|E|)$ is our sought after partial vibrational density of states (PVDOS) and β is the thermodynamic beta (β=K_BT)$^{-1}$. However, our obtained spectrum includes

higher-order phonons and we must isolate the single-order phonons to extract $g(s,|E|)$. Here it is critical to note that from eq. (9.18) the excitation probability for a single phonon event is limited by $E\left(1-e^{-\beta E}\right)$; this implies high-energy single-phonon features will be difficult to observe. The general excitation probability is then described with recursive phonon convolutions for $n\neq1$:

$$S_n(s,E)=\frac{1}{nf}\int S_{n-1}\left(s,E'\right)S_1\left(s,E-E'\right)dE' \tag{9.19}$$

Integration of eq. (9.19) for all energy space allows for the total excitation probability as a function of phonon order:

$$P_n=\frac{f(-\ln f)^n}{n!} \tag{9.20}$$

which is identical to eq. (9.9). Here, we can see dominance in the first-order contribution to the probability as f approaches one, the $(-\ln f)$ term gets smaller. Conversely, for low f we see a rise in the higher-order phonon contribution. We can simplify the convolution in eq. (9.19) to multiplication through Fourier transformation:

$$\tilde{S}_n=\frac{f}{n!}\left(\frac{\tilde{S}_1}{f}\right)^n \tag{9.21}$$

This transformation is useful as the higher-order phonon excitation probabilities still depend recursively on (the Fourier image of) the single-phonon excitation probability. Then the Fourier image of the total energy-dependent excitation probability follows as:

$$\tilde{S}=f+\sum\tilde{S}_n=fe^{\frac{\tilde{S}_1}{f}} \tag{9.22}$$

Now we can extract the single-phonon excitation simply by solving for S_1 through inversion

$$S_1=\mathcal{F}^{-1}\left[f\ln\left(\frac{\tilde{S}}{f}\right)\right] \tag{9.23}$$

where $\mathcal{F}^{-1}$ is the inverse Fourier-transform operator. This form of the function is more advantageous as it is dependent on Fourier image of the excitation spectrum $\tilde{S}$ and a physical property, f. Now we can relate eqs. (9.18)–(9.23) to solve for the PVDOS, $g(s,|E|)$, using accessible properties/observables E, E_R and β

$$g(s,E)=\frac{E}{E_R}\tanh\frac{\beta E}{2}\ \left(S_1(s,E)+S_1(s,-E)\right) \tag{9.24}$$

However, an exact vibrational density of states need not follow any simple expression. The Debye PVDOS increases as the square of the frequency (or energy) until it cuts off abruptly at the Debye frequency, ω_D:

$$g(\omega) = \frac{9\omega^2}{\omega_D^3} \quad or \quad D(E) = \frac{9E^2}{E_D^3} \tag{9.25}$$

If we incorporate a variety of typical numerical values for a Debye function into the above single-phonon formula (eq. (9.21)), the resulting single phonon excitation spectra are illustrated in Figure 9.7.

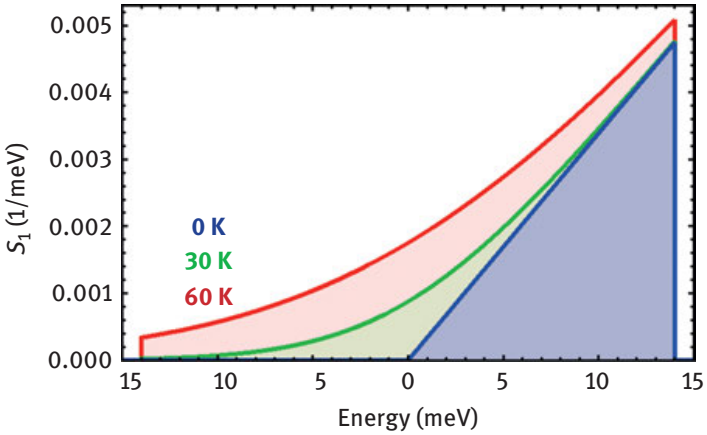

Figure 9.7: Single-phonon excitation probabilities, $S_1(E)$, for a Debye model PVDOS with a cutoff energy of 14 meV at different temperatures.

9.2.6 Other quantities from NRVS analysis – sum rules

As we mentioned earlier, there are several physical properties that can be extracted from NRVS spectra. A short list is included in Table 9.1. Many of the useful quantities are obtained from the so-called sum-rule analysis, where the sum relies on integrals yielding various moments of the excitation spectrum [7]. Specifically, the nth moment is defined as $W_n = \int E^n S(E)\, dE$ (here we use W_n instead of S_n to avoid confusion with the n-phonon absorption probability).

The first rule involving the 0th moment is trivial – the sum of probabilities over all possible events is 100% – something must happen. Thus, by definition, the zeroth moment W_0 is the integrated transition probability and hence unity:

$$W_0 = \int S(E) dE = 1 \tag{9.26}$$

Table 9.1: Summary of the properties extracted by different spectral moments.

W_0	1	By definition of probability
W_1	E_R	Recoil energy – independent of chemical environment
M_2	$4E_R K_{\text{av}}$	K_{av} is the average kinetic energy
M_3	$\frac{\hbar^2}{m} E_R\, k_{\text{av}}$	k_{av} is the average force constant

As we have seen from eq. (9.15), the first moment is useful because it turns out to be independent of the chemical environment of the nucleus under study – it just depends on the recoil energy E_R:

$$W_1 = \int ES(E)\, dE = E_r \tag{9.27}$$

This expresses a satisfying result: the average energy transfer to the lattice is equal to the recoil energy of the free atom. Since the recoil energy is already known from $E_R = E_0^2/2mc^2$, the above equation turns out to be a convenient tool for normalization of the overall spectrum.

The next two sum rules are simpler if one uses "centered moments" defined as

$$M_n = \int (E - E_r)^n S(E) dE \tag{9.28}$$

The centered second moment provides the average kinetic energy K_{av} of the nucleus under study:

$$M_2 = \int (E - E_R)^2 S(E)\, dE = 4E_R K_{\text{av}} \tag{9.29}$$

Finally, the centered third moment turns out to be proportional to the average force constant K_{av} holding an atom in its position along the average photon direction $\hat{k}$:

$$M_3 = \int (E - E_R)^3 S(E)\, dE = \frac{\hbar}{m} E_R k_{\text{av}} \tag{9.30}$$

We summarize by stating an obvious but nice fact about sum rule analysis – it requires far fewer presuppositions than building a normal mode model based on a hypothetical force field.

9.3 The NRVS experiment

Although the recoil fraction may have an overall cross section comparable to the recoil-free fraction, the intensity is spread over tens or hundreds of meV, compared to tens of neV for the Mössbauer effect. Thus, the absorption cross section at any particular energy is effectively six orders of magnitude weaker than that of the elastic resonance. So how is it ever possible to observe the NRVS effect? The key to the synchrotron experiment is to *exploit the time delay for the emission of nuclear fluorescence and internal conversion X-ray fluorescence* while ignoring unrelated faster electronic scattering events. Of course, having a high-brightness source and a HRM system is also essential [45]. A typical NRVS experimental setup is illustrated in Figure 9.8 and in this section we will discuss the role of each major component in the setup.

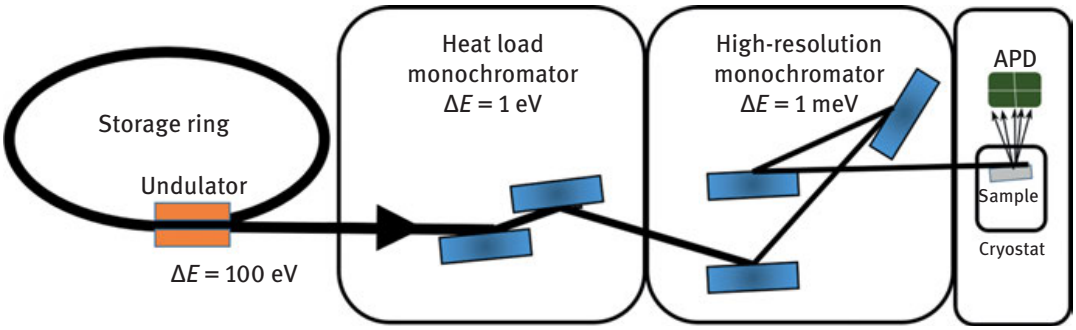

Figure 9.8: Schematic setup of an NRVS experiment.

Not every Mössbauer isotope is suitable for an NRVS experiment. First, one needs a monochromator with sufficiently narrow bandpass to resolve vibrational features, generally ~ 1 meV resolution. Currently, this limits the nuclear resonance energy to <40 keV. Second, the nuclear excited state lifetime must be long enough to allow the detector to distinguish nuclear events from "prompt" electronic events, but short enough to be accommodating to the synchrotron period and bunch frequency. The isotopes that have made the cut so far are illustrated in Figure 9.9. Currently, lifetimes from hundreds of ps to hundreds of ns are feasible. Fortunately for many materials and biological applications, one of the most accommodating isotopes for NRVS is ^{57}Fe.

9.3.1 Comparison to Inelastic Scattering Spectroscopy

NRVS is often considered a NIS spectroscopy. For inelastic spectroscopies, it is key to measure the incident E_1 and scattered energies E_2 to accurately define the energy transfer ($E_1 - E_2$), and extract the inelastically scattering signal from the significantly

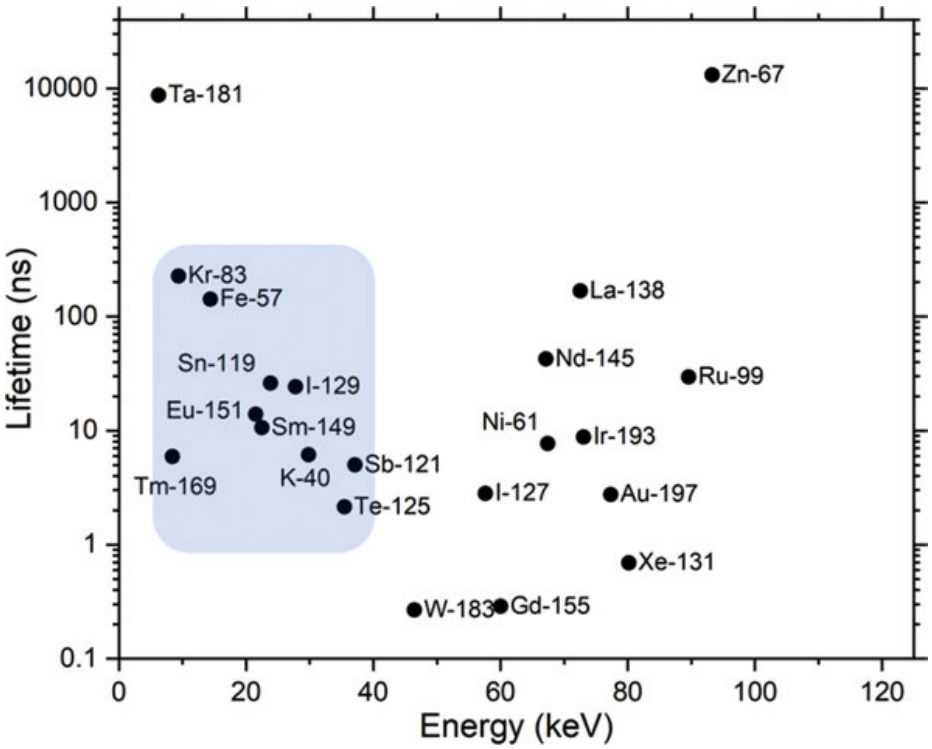

Figure 9.9: Energies and lifetimes of some nuclear isotopes with the shaded region indicating lifetimes and energies that are amenable to current synchrotron technology. Values obtained from the International Atomic Energy Agency Nuclear Data Service website (www-nds.iaea.org).

larger background. As will be discussed later, a narrow band incident energy can be provided via a HRM – where 1 meV is considered reasonable resolution for observing vibrational features. For conventional scattering spectroscopies like resonance Raman, the detection of the scattered radiation is well resolved relative to the incident beam. Also, inelastic X-ray scattering (IXS) utilizes energy-resolved detection of scattered photons that can be on the same energy scales as NRVS.

In the case of measuring NRVS, since the nuclear Mössbauer transitions often have a very narrow linewidth (~5 neV for ^{57}Fe), the nuclear transition itself provides an excellent point of reference for the E=0 in terms of vibrational energy. NRVS measures the elastic Mössbauer transition then tune the incident energy into the inelastic sidebands; thus, measurements do not utilize an energy analyzer for scattered photons, which makes this spectroscopy have a much higher photon out throughput than scattering experiments. For example, IXS uses an incident beam flux in the order of 10^{10} photons/s and produces ~1 cts/s (counts per second) for the asymmetric Fe–Cl stretch at 380 cm^{-1} in a $[FeCl_4]^-$ sample; NRVS uses a beam flux on the order of 10^9 photons/s and has ~10 cts/s of signal for the same vibrational feature. This advantage makes NRVS preferable (e.g., vs IXS) for biological

measurements because it leads to a higher signal level while having a lower amount of incident radiation dose on samples.

Although the scattered energy can be well defined by the nuclear transitions themselves, the photons collected by the detector(s) include not only the signal from the nuclear scattering event but also the unwanted background counts from the electron scattering (in the order of millions of cts/s per detector). Since NRVS uses no energy analyzer, it is necessary resolve the signal from the background via another option: time. Fortunately, the nuclear scattering process has a long lifetime on the order of ns (e.g., ^{57}Fe at 14.4 keV has a 1/*e* lifetime of 141 ns), whereas X-ray-electron interactions are essentially instantaneous on this time scale, leaving the background's pulse duration the same as the SR's pulse duration (e.g., 70 ps). This makes it possible to distinguish the nuclear scattering contribution from the electron scattering background in the time domain. A practical description of this procedure will be discussed in later sections.

9.3.2 X-ray sources for NRVS

9.3.2.1 Synchrotron radiation sources

SR is the electromagnetic radiation emitted when electrons are accelerated radially while at relativistic speeds. In practice, the electrons are traveling along a circle, the acceleration is perpendicular to the velocity ($a \perp v$) and the radiation is along the tangent direction of the circle via an insertion device such as a bend magnet, wiggler or undulator. SR has many advantages, such as high flux / brilliance, high linear, elliptical or circular polarization, small angular divergence, low emittance (i.e., the product of source cross section and solid angle of emission is small), wide energy tunability and pulsed time structure. These advantages have lead to many advanced applications in areas from condensed matter physics to biology, from academic research to industrial technologies.

There are more than 100 SR rings around the world; however, most of them are suitable for NRVS measurements. The ideal narrow incident bandwidth (on the order of 1 meV) demands a specialized X-ray optics called an HRM, and the other NRVS requirements depends on the type of SR rings. For measuring ^{57}Fe nuclei (1/*e* lifetime = 141 ns), a radiation pulse interval of ~150 ns is optimal. SR rings support multiple experimental techniques at end stations with differing requirements of flux, bunch spacing and bunch width. NRVS requires a large storage ring capable of widely spaced bunches and/or hybrid bunch modes (sections of electrons with differing bunch timings). It also requires a high energy electron beam to create sufficient flux at high X-ray energies. Currently four storage rings in the world are set up to allow NRVS experiments (Table 9.2): APS in Chicago, USA (1.1 km, 7GeV, since 1995); SPring-8 in Hyogo, Japan (1.5 km, 8GeV, since 1996); ESRF in Grenoble,

Table 9.2: Beamlines, and their approximate operating conditions, that perform NRVS spectroscopy.

Facility/ beamline	Energy (GeV) [46]	Emittance (nm-rad) [46]	Period (mm)	# of periods	Flux (photon s^{-1})/ resolution (meV) (at 14.4keV)	Possible isotopes
ESRF ID-18	6	3.0	20 [47]	60 [47]	3.6×10^9/0.84 meV [47] 1.3×10^9/ 0.47 meV [47]	^{57}Fe, ^{151}Eu, ^{149}Sm, ^{119}Sn, ^{161}Dy, ^{121}Sb, ^{125}Te, ^{129}Xe
APS 3-ID-D	7	3.1	27 [48]	88 [48]	5×10^9/1 meV [49]	^{57}Fe, ^{151}Eu, ^{83}Kr, ^{119}Sn, ^{161}Dy
SPring-8 BL09-XU	8	3.4	32 [50]	140 [50]	1.9×10^9/0.8 meV [51] 2.5×10^9/1.1 meV [52]	^{57}Fe, ^{151}Eu, ^{149}Sm, ^{119}Sn, ^{40}K, ^{125}Te, ^{121}Sb
SPring-8 BL19-LXU	8	3.4	32 [50]	780 [50]	~6×10^9/0.8 meV [53]	
PETRA III P01	6	1	32 [54]	314 [54]	12×10^9/1.0 meV [55]	^{57}Fe, ^{119}Sn, ^{121}Sb, ^{121}Te, ^{193}Ir

France (0.9 km, 6 GeV, since 1994) and Petra-III in Hamburg, Germany (2.3 km, 6 GeV, since 2010).

9.3.2.2 Undulators and monochromators

For NRVS specifically, the incident beam is invariably generated by a set of magnets called an undulator. In an undulator the radiation from different poles constructively interferes with the motion of the oscillating electrons resulting in a narrow beam energy profile. A useful metric that characterizes a wiggler/undulator is the K-factor:

$$K = \frac{eB\lambda_u}{2\pi m_e c} \tag{9.31}$$

where e is the charge of the electron, B is the magnetic field strength of the insertion device, m_e is the electron rest mass and λ_u is the period of the magnetic oscillation. The K-factor characterizes the oscillation amplitude of the particle – for K much greater than 1 the oscillation is amplitude is large and behaves like a wiggler. For K-factors much less than 1, we see the interference characteristic of an undulator. Changes in K alter the energy profile of the beam, and we can achieve the

desired K by tuning the magnetic field, B. This is accomplished by modifying the "undulator gap" between the magnets above and below the electron path.

The primary advantages of using an undulator include a narrow angular divergence, a high brightness and a narrow energy distribution. The white light from an undulator at an NRVS beamline has a bandwidth on the order of 100 eV of width in energy. The gap is tuned specifically for a desired experimental energy range. As NRVS is obtained over a range of 100s of meV around a central energy on the order of keV, the undulator gap is usually not changed during the course of an experiment. The initial beam is narrowed further by a liquid nitrogen or water-cooled high heat load monochromator (HHLM), which reduces the radiation energy to about 1 eV in bandwidth, before reaching the end-station of the beamline the beam is further reduced to ~1 meV by a HRM. There are also many optics and mechanical components that shape/focus the beam. With so many requirements, experimental end-stations at NRVS beamlines tend to be 25–100 m away from the SR ring.

9.3.2.3 High-resolution monochromators

Crystals diffract X-rays with different energies at different angles characterized by Bragg's law:

$$n\lambda = 2d\ \sin\theta \tag{9.32}$$

where n is the order of diffraction, λ is the wavelength of energy being diffracted, d is the spacing between crystal planes and θ is the scattering angle. This wavelength scattering angle relationship is utilized in the design of crystal monochromators. Regular diffraction refers to the case in which the incident and the diffracted beams are symmetric with respect to the crystal's cut surface, for example a Si(1,1,1) crystal used in a heat load monochromator at an NRVS beamline. On the other hand, asymmetrical diffraction means that the cut surface of the crystal is not in parallel with the diffraction crystal plane and therefore the incident and diffracted X-rays are not symmetric with respect to the crystal's cut surface. An asymmetric diffraction can obtain a larger beam broad angular acceptance of the input beam and narrow dispersion of the output beam ($D_i \rightarrow D_o$) than a symmetric diffraction while outputting a larger beam size beam size ($S_i \rightarrow S_o$), as shown in Figure 9.10. The ~1 meV bandwidth X-ray beam used for NRVS measurements can be produced via a pair of such asymmetrically cut and high reflection index such as Si(9,7,5). To further disperse the beams with different energies, the normal angles of these two diffraction crystal planes are arranged between 90^o–180^o, forming a ++ (dispersive) crystal array. The pair of asymmetric crystals are referred to as the *key diffractive crystals*.

At SPring-8 BL09XU, for ^{57}Fe NRVS a three-crystal HRM is utilized, in which a pair of Si(9,7,5) crystal planes were chosen as its key diffractive crystal surfaces, and a Ge (3,3,1) crystal is used as a front mirror to adjust the direction of the input optical path.

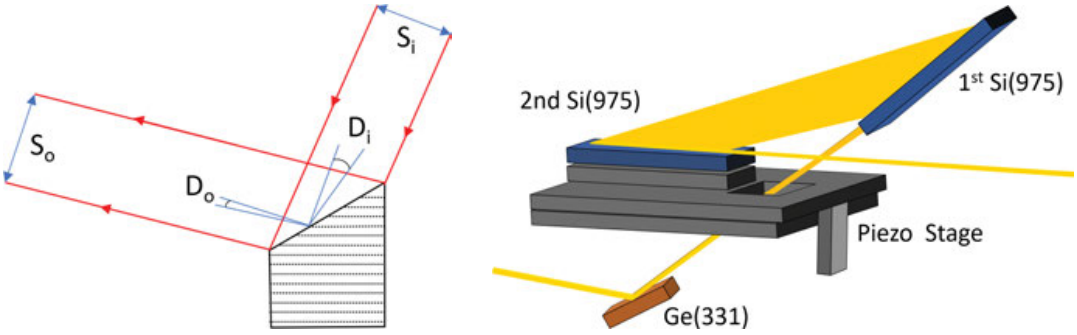

Figure 9.10: Left: A schematic of an asymmetrically cut monochromator crystal plane. Right: A diagram of the three-crystal HRM at BL-9XU at SPring-8.

APS 03ID implements a four-crystal HRM with its key crystal plane being Si(10,6,4), and the front and back manipulation crystals being Si(4,0,0); the latest Petra-III P01 nuclear scattering beamline also uses a 2Si(10,6,4)×2Si(4,0,0) HRM setup for ^{57}NRVS. The three-crystal HRM usually produces a beam with 0.1 × 0.6 mm^2 in cross section, while the four-crystal one produces a cross section of 0.1 × 0.1 mm^2. Some beamlines have Kirkpatrick–Baez focusing mirrors to produce a beam in even smaller sizes. So far, either a four- or a three-crystal HRM can provide X-rays that have ~1 meV energy resolution or better at energies (5–30keV) suitable for many NRVS experiments.

9.3.2.4 About energy calibration

Monochromator crystals can expand or contract due to fluctuations in ambient temperature. Although these environmental variables are usually controlled well at an SR facility, the precise location of the nuclear resonant peak position and the stability of the energy axis scale must be calibrated. The nuclear resonant peak can be calibrated as 0 meV with respect to vibrational quanta during data analysis. However, the energy values relative to monochromator motion still need to be calibrated with a standard sample. As shown in Figure 9.11, the $FeCl_4$ T_2 stretch peak from the same complex sample $[NEt_4](FeCl_4)$ measured at different beamlines do not overlap and vary by up to 4 meV with each other. A linear correction factor (the energy axis scale) of about 0.920–1.005 can bring all of the uncalibrated spectra into very good alignment with the reported Fe–Cl T2 peak centroid (at 380 cm^{-1}).

The primary source of energy uncertainty in the monochromator comes from changes in the crystal plane *d*-spacing due to temperature. For Si, the coefficient of thermal expansion is 2.56 × 10^{-6} K^{-1}, leading to an energy shift of 9 cm^{-1} (or over 1 meV) per 0.03 K of temperature change. Inadvisably entering the monochromator hutch could change the crystal temperature by 0.1%. This could lead to a several meV energy drift and require hours to re-equilibrate. Therefore, beamline energies

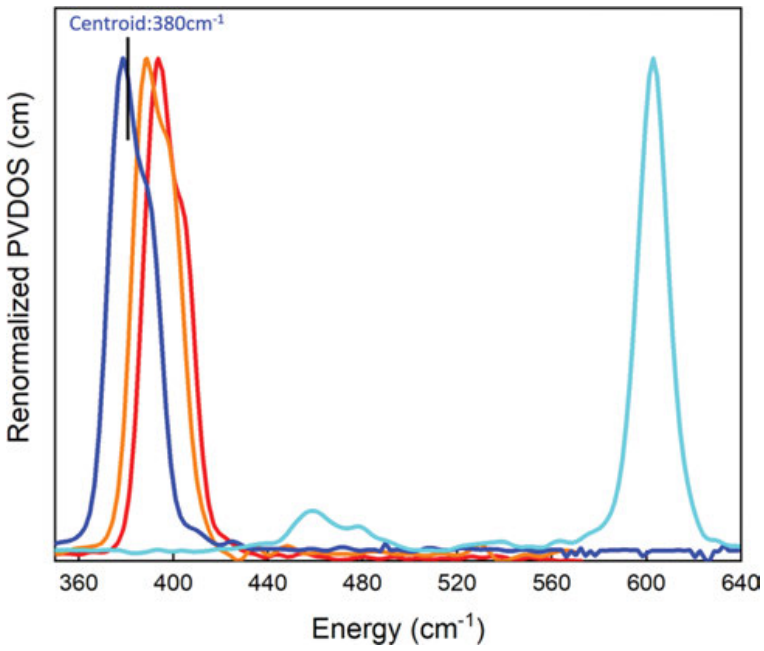

Figure 9.11: NRVS PVDOS spectra for the calibrated $(NEt_4)FeCl_4$ ion (——). An uncalibrated spectrum measured in May 2015 at BL09XU (——) and the same sample measured seven day later (——). Also, the room temperature PVDOS spectrum for $(NH_4)_2MgFe(CN)_6$ (——) as an alternative higher-energy calibrant. Major peaks renormalized from 0 to 1 for illustration.

must be frequently checked especially when the temperature of the hutch is disturbed.

However, it should be noted this temperature sensitivity can be intentionally used as a mechanism of tuning monochromator energy. For example, the sapphire backscattering HRM at Petra-III P06 is tuned by temperature scanning and it allows access to nuclear resonances above 30keV with ~1meV resolution.

The energy calibration becomes more critical for dilute biological NRVS measurements as the acquisition times can be long (>24 hours) and both the zero position and the energy scale will drift more. As sample changes take time (1 hr), the traditional energy calibration interrupting an extended biological sample measurement may not be desirable. To resolve this issue, the calibration can also be done via measuring ^{57}Fe powder at 285 cm^{-1} or $(NH_4)_2MgFe(CN)_6$ at 602 cm^{-1} at room temperature (RT) in a separate stage outside the back of the cryostat stage (similar to in situ foil calibrations used for EXAFS measurements). The calibration at this second stage can be a quickly switched to by letting the full beam bypass to the main stage (the cryostat chamber), or an *in situ* measurement that is done at the second stage while the biological sample is measured at the main stage; however, this is not recommended as it increases the mechanical deadtime of the overall measurement.

9.3.3 Detecting NRVS

As discussed previously, the most important factor for separating the NRVS signal from the prompt electronic scattering background is time resolution.

9.3.3.1 Avalanche photodiode detectors

Avalanche photodiode (APD) detectors possess properties that are suitable for measuring NRVS. The saturation level for an APD is about 6 MHz per APD element no matter how large the element area is. Therefore, using an APD array with small individual elements instead of a single APD is advantageous. Figure 9.12 (top) shows an example of 2 × 4 APD array used in SPring-8 BL09XU. The combined high-gain and high-saturation rate makes APDs suitable for measuring the NRVS, which has a weak signal but a large background at the same time.

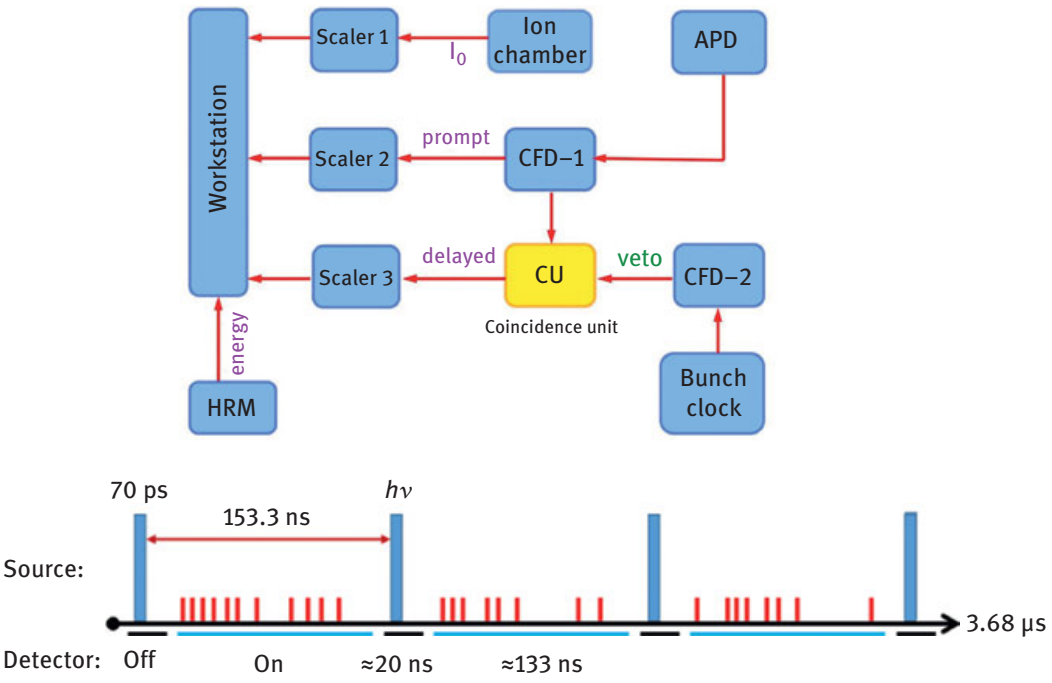

Figure 9.12: Top: Electronics used to separate delayed nuclear events from prompt -ray events. Middle: A typical timing scheme for an NRVS experiment. Detector "off" implies the counts are not being sent to "Scaler 3" in the top diagram. The specific times are typical for APS operating conditions. Bottom: Close up image of an APD array with inset being a zoomed in picture of the individual APD elements.

Modern APDs can have a time resolution of 1 ns or better, which is good for many types of NRVS experiments, including those on ^{57}Fe.

9.3.3.2 Data-acquisition electronics

APDs collect the photons but it is the data-acquisition electronics that finally separate the delayed nuclear signal from the prompt background in the time domain. A block diagram for the data-acquisition electronics is shown as in Figure 9.12 (top) to illustrate this process. One important device is the "bunch clock," which tells the electronics the initial time point of $t = 0$ when a synchrotron pulse arrives. When both the APD and bunch clock send pulses to the CU simultaneously, the latter passes the signals from the APD, which is then digitized and sent to the workstation for storage. In practice, a veto interval X is set around $t = 0$ (where X is about ±10 ns), to avoid the signal integration during this period and to allow the electronics to recover from the enormous background pulse. Then, the counts for the events that occur between $t = X$ and $150 - X$ (e.g., $t = 10$–140 ns) is passing through the CU and digitized as NRVS counts. The values without time structure, for example, I_0, prompt and energy positions are directly digitized to send to the workstation for storage.

9.4 Data analysis

9.4.1 Data processing

To compare theory and actual experiment, we need to be able to proceed in the opposite direction – extraction of the PVDOS from the experimental data. A variety of programs are available for the analysis of NRVS spectra, including DOS [57] and PHOENIX [58]. The key steps in the analysis of NRVS data are as follows:

- determination of the resolution function $R(E–E')$,
- normalization using sum rules,
- subtraction of the elastic component,
- decomposition into n-phonon contributions and
- derivation of the PVDOS.

Herein we briefly summarize the steps taken by the PHOENIX software [34]. For actual experimental data the measured intensity transforms from eq. (9.17) to:

$$I(E) = \int R\left(E - E'\right)\{aS(E) - b\delta(E)\}dE' \tag{9.33}$$

We have distributed the normalization constant A into a and b and have introduced the experimental monochromator resolution function $R\left(E - E'\right)$. Next, the resolution function must be precisely fit to the spectrum. The high statistics of the elastic peak give an obvious target to fit the resolution function; however, the contribution to

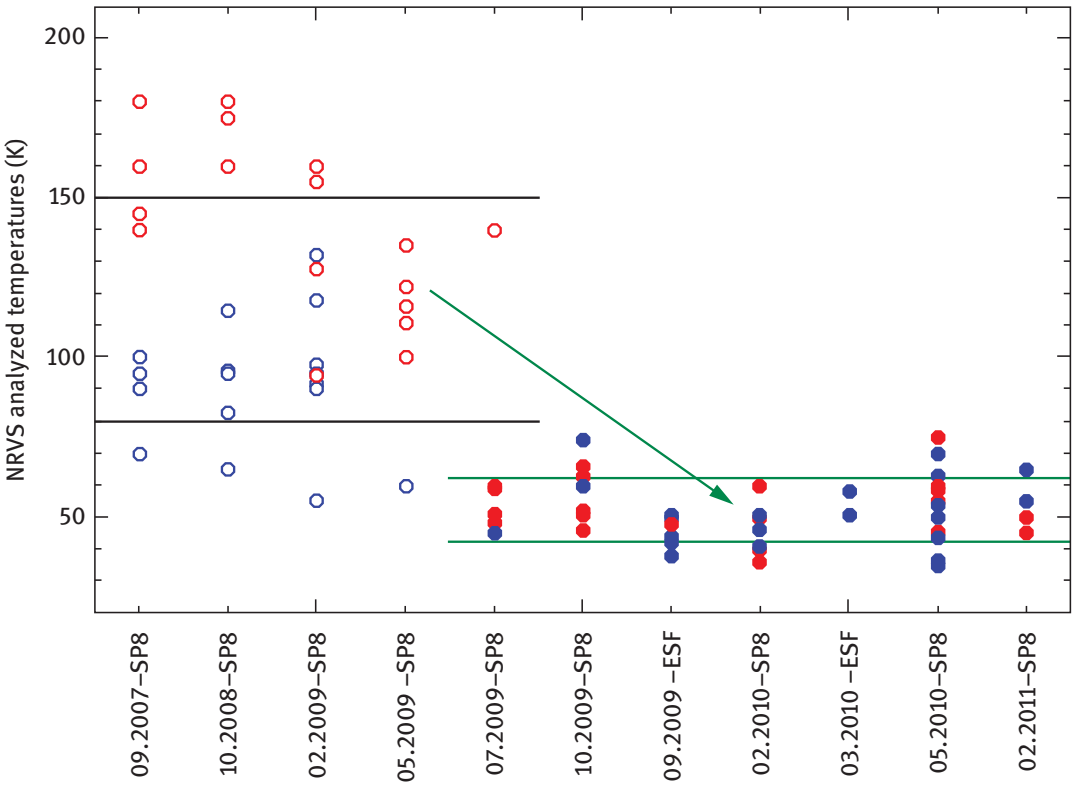

Figure 9.13: Real sample temperature during different beamtimes from 2007–2011 at SPring-8 (SP8) and ESRF. Red points are biological samples and blue points are solid samples – filled points represent samples that were attached to the cryostat by 1-propanol and open points were attached by cryogenic grease.

the area under the elastic peak also comes from the inelastic contribution – here estimated as a Debye solid – so the following function is fitted:

$$P(E) = c_1 \left\{ R(E - c_0) + \frac{c_2 \beta (E - c_0)}{\left(1 - e^{-\beta (E - c_0)}\right)} \right\} \tag{9.34}$$

All c terms are variable fitting parameters. The term c_0 allows for adjusting the position of the resonance, c_1 scales the height of the function to the elastic peak and the term c_2 adjusts the phonon contribution. The function $R(E - c_0)$ provides the resolution function as follows:

$$R(E) \begin{cases} = H\left[E\frac{2c_3}{1+c_4}\right], & E \geq 0 \\ \quad H\left[E\frac{2c_3c_4}{1+c_4}\right], & E < 0 \end{cases} \tag{9.35}$$

where $H(x)$ is a generic shape function:

$$H(x) = e^{-|x^{c_5}|} \tag{9.36}$$

All c values are fit using a least squares minimization. Next the first moment of the spectrum is normalized to the recoil energy according to eq. (9.18) determining the normalization factor a. From eq. (9.24) we see that the Lamb–Mössbauer factor must be determined for the eventual deconvolution. Utilizing the normalization factor, fitted elastic peak and resolution function, we can solve for the elastic contribution to the experimental spectrum:

$$f = 1 + \frac{c_1}{a} - \frac{1}{a}\int I(E) - c_1 R(E) dE \tag{9.37}$$

Finally, PHOENIX performs the Fourier-log deconvolution [59] a modification of eq. (9.23):

$$S_1(E) = f\mathcal{F}^{-1}\left[\tilde{R}\ln\left\{1 + \phi\frac{\tilde{I} - c_1\tilde{R}}{af\tilde{R}}\right\}\right] \tag{9.38}$$

Here $\tilde{R}$ is the Fourier image of the resolution function and $\tilde{I}$ is the Fourier image of the normalized intensity spectrum. Likewise, PHOENIX calculates higher-order phonons. The term ϕ is a mollifier function that convolutes with the subtracted spectrum to limit Fourier artifacts.

$$\phi = \min\left\{1, \left|\frac{\tilde{I}\tilde{R}(0)}{\tilde{R}\tilde{I}(0)}\right|\right\} \tag{9.39}$$

The final PVDOS is calculated identically to eq. (9.24).

From a practical standpoint, the energy axes of multiple scans are aligned based on their position of the elastic resonance, then a calibration factor is applied. As mentioned previously, this approximately linear factor can be determined by the position of three prominent peaks for $[Et_4N]FeCl_4$ (Figure 9.3). It can also be determined by fitting the Stokes and anti-Stokes regions for a sample of accurately known temperature [60].

9.4.2 Data interpretation

Once the NRVS-derived PVDOS is in hand, the interpretation depends on the problem of interest. However, among the interpretive approaches employed are as follows:

- sum rule analysis for physical observables,
- graphical analysis for speed of sound,
- isotope shifts,
- optimization of empirical force fields,

- group theory and
- interpretation via density functional theory (DFT) calculations.

As discussed previously, the sum rules provide a straightforward prescription to obtain physical observables such as the Lamb–Mössbauer factor and average force constant of the probe atom. Albeit less obvious, the speed of sound through the material can be obtained by graphical manipulation and extrapolation.

Due to the selectivity of NRVS for the probe isotope motion, many features in a spectrum can be initially assigned based on a combination of chemical intuition, literature precedents and group theory. To further refine the assignments, isotopic substitution can be employed to highlight modes involving the substituted atom motion. A normal coordinate analysis can also be employed that generates a spectrum from a set of internal coordinate force constants. The resulting force field can then be optimized to reproduce the experimental spectrum affording information about the strength and motion of vibrational modes, which, if symmetry allows, can be related back to group theory [61].

In recent years, DFT calculations have prevailed as a straightforward way to interpret vibrational spectra. For NRVS, first principle calculations of PVDOS are derived from the orthogonal matrix that diagonalizes the mass-weighted second derivative Hessian matrix [62]. The basic procedure is routinely performed by many quantum chemistry codes during the calculation of vibrational frequencies and modification to yield the PVDOS for the probe atom(s) is straightforward.

9.5 Application to model complexes

In metal complexes, metal–ligand stretching and bending frequencies range from ~50–2,000 cm^{-1}, or ~6–250 meV. NRVS is exciting, in part because it provides an isotope selective vibrational spectrum. In the case of Fe NRVS, only modes that involve displacement of the ^{57}Fe nucleus couple to the nuclear transition.

9.5.1 Coordination complexes

9.5.1.1 Fe_2O_2

Peroxo diiron complexes, abbreviated here as Fe_2O_2, are common intermediates in biological binuclear Fe oxygenases. Key to understanding the underlying biological chemistry is characterizing the binding moiety of the peroxo bridge. There are numerous possibilities for a peroxide bridge to form between two irons: a cis 1,2 bridge, a trans 1,2 bridge, two doubly bridging oxygens, a bridging plus terminally bound oxygen and a bridging oxygen with the distal oxygen not bound to either

iron. NRVS spectroscopy can be utilized to understand the iron-bound peroxo species in biological intermediates, especially where Raman and/or structural data are not available. To understand how the peroxo-binding moiety affects the molecular vibrations of the diiron site, NRVS was utilized on a model complex, $[Fe_2(\mu\text{-}O_2)(N\text{-}EtHPTB)(PhCO_2)]^{2+}$ (abbreviations available in reference) [63].

As shown in Figure 9.14, the NRVS spectrum of the peroxodiiron model is dominated by an envelope of features from 150–300 cm^{-1}; these modes are dominantly Fe-(N-EtHPTB/$PhCO_2$) in nature. The region from 440–480 cm^{-1} is of special interest and the features in the natural abundance (O_2) spectrum at 446 and 458 cm^{-1} clearly shift to 446 and 458 cm^{-1} in the ^{18}O sample. Likewise, the shoulder centering at 338 cm^{-1} also shifts inward to 311 cm^{-1} in the ^{18}O isotopologue.

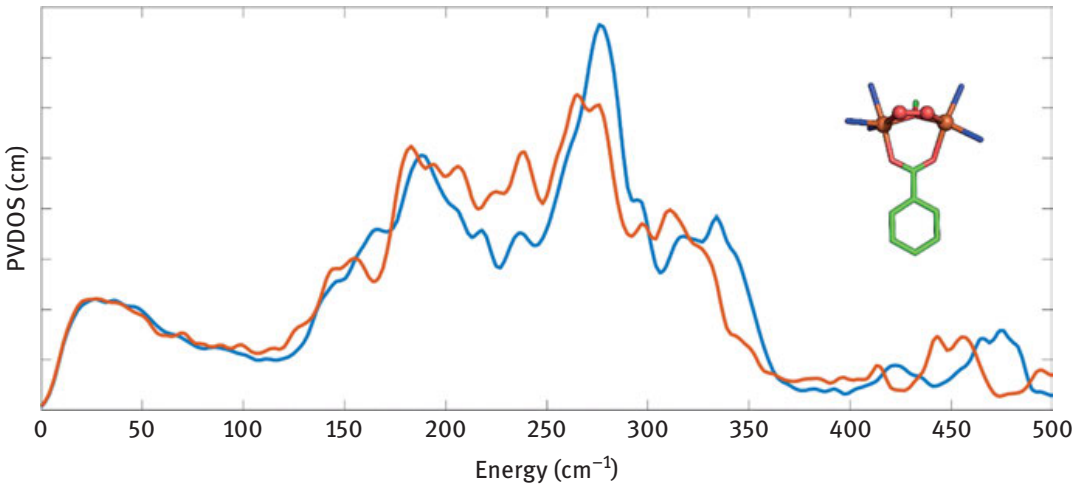

Figure 9.14: NRVS spectra for the $^{57}Fe_2(\mu\text{-}O_2)(N\text{-}EtHPTB)(PhCO_2)$ (——) and ^{18}O substituted compound (——). Inset, truncated image of the Fe_2O_2 site and neighboring atoms.

The isotope shifts, empirical force field analysis and group theory identified the higher energy features. The observed pair of highest energy peaks were characterized as a Fermi doublet [64, 65] with dominantly Fe–O–O–Fe symmetric stretching motion. The isotope-sensitive intensity centered at 325(313) cm^{-1} was not previously observed in resonance Raman. To describe this motion, the spectrum was simulated with the program Vibratz [61]. Using a set of internal coordinate force field constants it was found that the feature was a result of coupled motion of the O–O group parallel to the Fe–Fe axis and perpendicular to a pseudo-mirror plane bisecting the four atoms later referred to as a "peroxide rock."

The study did not elaborate on the modes in the 150–300 cm^{-1} region, but was comprehensively built upon in a later study [66] where DFT was utilized to describe the region as a combination of "core motions," peroxide twisting motion and a "butterfly" motion where the oxygens move perpendicular to the Fe–O–O–Fe plane

in opposite motion to the irons. Collectively, the distribution of these modes in the spectrum are related to the deviation of the bridging alkoxide oxygen atom from the Fe–O–O–Fe plane created by the bridging peroxide.

These studies established correlations between NRVS spectra and structure that would be translated to the study of biological peroxo-bound diiron systems; specifically the P′ peroxo-bound intermediate of the AurF enzyme [67].

9.6 Applications to biological systems

9.6.1 Rubredoxin

The relatively simple metalloprotein, rubredoxin, contains a single Fe center coordinated to four cysteine amino acid residues. The two accessible redox states of the Fe site are formally Fe(II) and Fe(III), which facilitate the electron transfer activity of the protein. The simplicity of the Fe site and ease of handling of the protein made rubredoxin an excellent early candidate for bioinorganic ^{57}Fe NRVS [68].

The NRVS spectra for the oxidized and reduced forms of the protein are shown in and are qualitatively dominated by the three peaks. For the Fe(III) site the peaks are centered at 70, 150 and 360 cm^{-1}. Although the reduced protein spectrum is similar to its oxidized counterpart, the high-frequency envelope downshifts to 303 cm^{-1}. The original work implemented the Vibratz program for empirical force field-based modeling to derive the Fe–S force constants. The crystal structures (reduced PDB:1CAD [69], oxidized PDB:1BQ8 [70]) were used as models for the simulations. The result was a calculated 36% decrease in Fe–S bond force constant (1.24 to 0.92 mdyne/Å) upon reduction of the protein.

The peaks were assigned using the vibrational mode description from the Vibratz modeling. For the oxidized protein model, the broad region from 345 to 375 cm^{-1} is composed of three strong components at 375, 358, 350 cm^{-1} and three weaker contributions at 365, 364 and 340 cm^{-1} that are principally described as Fe-S asymmetric stretching modes. The intensity in the region from 300 to 340 cm^{-1} arises from nearly symmetric Fe–S stretch modes. It would be expected that a perfect symmetric stretch would not cause Fe motion; however, the intensity is a consequence of the deviation from ideal symmetry. The contribution in this so-called breathing region is approximately 10% that of the asymmetric stretch components. The region near 150 cm^{-1} is composed of nearly degenerate S–Fe–S bending modes. The region between 100 and 150 cm^{-1} is assigned as Fe–S–C bending modes with mixing of S–Fe–S modes. Finally, the low-energy region below 100 cm^{-1} involves significant dihedral, torsional, acoustic and delocalized vibrational modes within the greater protein.

When the same analysis is performed for the reduced Fe center, the order of assignments remains the same, but the stretching modes downshift by 18%. It is noteworthy that the symmetric stretch centroid shifts to approximately 270 cm^{-1} and start to mix with the bending modes leading to enhanced intensity throughout the 150–300 cm^{-1} region (Figure 9.15).

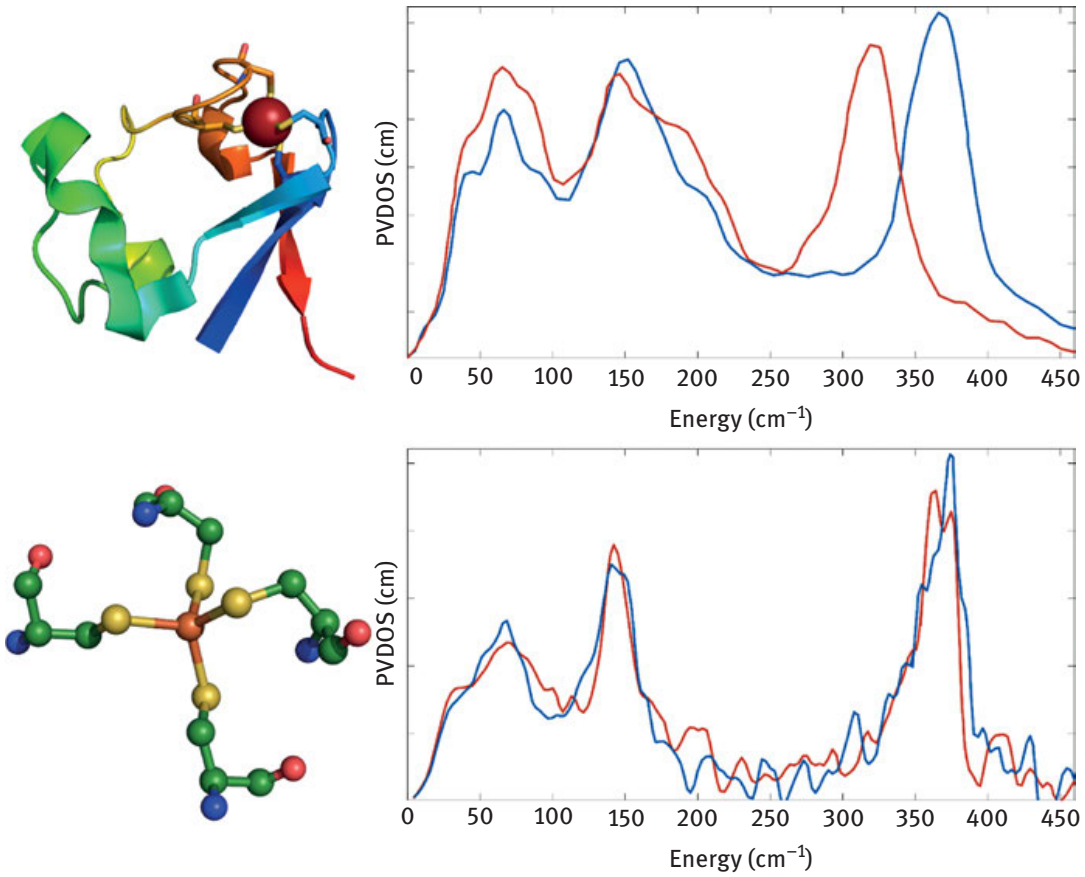

Figure 9.15: Left top: The crystal structure of rubredoxin (pdb: 1CAD). Left bottom: The Fe site in rubredoxin and proximal cysteines. Right top: The NRVS spectra of the oxidized (——) and reduced (——) rubredoxin protein. The NRVS spectra of the oxidized ^{57}Fe rubredoxin aligned along the crystallographic *a*-axis (——) and the crystallographic *c*-axis (——). Figure reproduced from previous works [68, 71].

9.6.2 Single-crystal rubredoxin

A follow-up single-crystal EXAFS and NRVS study was performed with oxidized rubredoxin – the first time such a study was done for an Fe–S protein crystal [71]. As NRVS is orientation dependent (eq. (9.12)), the vibrational modes of a single crystal

of rubredoxin are enhanced when the ^{57}Fe motion is along the direction of the incident photon vector **K**. The three strong asymmetric stretch modes at 373, 358 and 352 cm^{-1} (corresponding to the modes at 375, 358 and 350 cm^{-1} in solution) were selectively enhanced by orientation of the incident photon parallel to the crystallographic *a*-axis and *c*-axis. Along the *a*-axis the average Fe–S bond length is 2.263 Å and 2.284 along the *c*-axis (determined by EXAFS). Projection of the incident beam on the *a*-axis enhanced the peak at 373 cm^{-1}, where orientation along the *c*-axis enhances the 358 cm^{-1} and completely hides the feature at 352 cm^{-1} (Figure 9.15 bottom right).

Vibrational modes in the Fe–S bending region of the rubredoxin crystal were less orientation dependent. The alignment on the *c*-axis enhanced the peak at 140 cm^{-1} and the *a*-axis orientation seemed to slightly split the peak. This implies that the ^{57}Fe bending normal mode motions are not "pure" projections onto the crystallographic axes.

The experiment was followed up by Vibratz modeling similar to the solution rubredoxin approach, but with an $Fe(SCC)_4$ model and an orientation dependent simulation. From the modeling, it is supported that the 352 cm^{-1} feature must lie perpendicular to the crystallographic *c*-axis. A key, but perhaps not surprising, observation made is that the highest frequency mode (373 cm^{-1}) enhancement is consistent with the crystallographic *a*-axis, which has the shorter average Fe–S bond length.

Collectively, the work demonstrates that single crystal NRVS coupled to EXAFS, or other structural methods, can be used to selectively probe individual vibrational modes and deconstruct vibrational envelopes. With the ultimate application of the work being to vibrationally uncouple systems containing multiple ^{57}Fe sites.

9.6.3 Non-Rieske [2Fe2S]

The logical continuation of the study of simple FeS clusters with NRVS was spectra obtaining for reduced and oxidized non-Rieske *Rhodobacter capsulatus* ferredoxin VI (Rc FdVI) [2Fe2S] cluster [72]. The [2Fe2S] cluster is characterized by two irons connected to the protein matrix by two terminal cysteinyl sulfurs (S^t) and connected to one another by two bridging sulfurs (S^b). In the oxidized form, the cluster is ferric and diamagnetic – whereas in the reduced form the cluster is a mixed ferric and ferrous antiferromagnetically coupled S=1/2 system. Unlike the single Fe counterpart in rubredoxin, the [2Fe2S] cluster in Rc FdVI has a sharper Fe–S stretching region with better-resolved components (Figure 9.16). The stretch region components in the all-ferric sample are observed at 421, 393, 352, 341 and 321 cm^{-1}. Raman spectra of [2Fe2S] clusters have a strong feature near 290 cm^{-1} that is not present in the NRVS corroborating the original assignment of the mode as a combination of two highly symmetric FeS_4 breathing modes with minimal Fe motion. It is useful to note that the redox sensitive Fe–S stretch modes greater

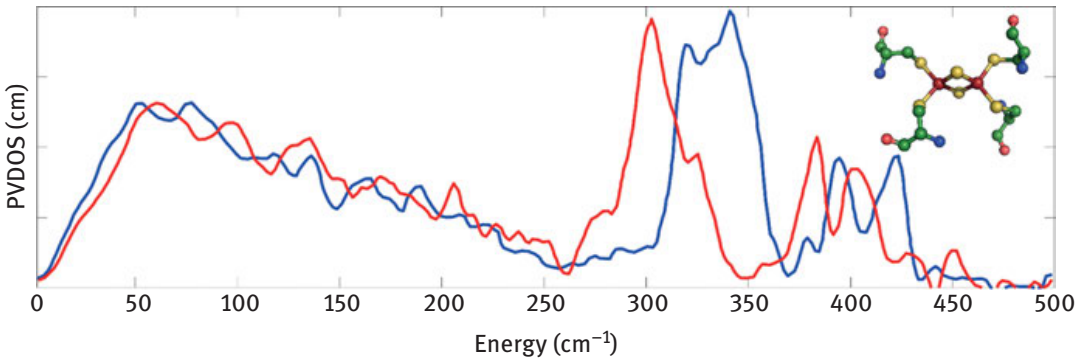

Figure 9.16: The ^{57}Fe NRVS spectrum of [2Fe2S] in the reduced (——) and oxidized (——) form. Figure reproduced from previous work [72].

than 400 cm^{-1} have become an identifier for [2Fe2S] clusters in systems with multiple clusters of varying composition [22].

The maximum of the oxidized protein NRVS spectrum occurs at 341 cm^{-1} in a region of broad unresolved components, while the highest frequency feature is found at 421 cm^{-1}. In the reduced protein, a spectral maximum occurs at 302 cm^{-1}. Likewise, the 393 cm^{-1} intensity shifts to 382 cm^{-1} in the reduced form. It is noteworthy that NRVS for the reduced protein was capable of observing a peak at 276 cm^{-1}, which was only predicted at the time to be a Raman unobserved Fe(II)–S^{t} stretch [73]. The spectrum for [2Fe2S] ferredoxin contains some resolvable features in the low-energy region below 250 cm^{-1}. However, since most of the intensity in this region involves numerous highly delocalized and weak vibrational motion that involve a sizable portion of the greater protein, they cannot be properly modeled using DFT or force field modeling using small model metalloclusters.

A Urey–Bradley force field simulation of the [2Fe2S] cluster spectrum was employed using Vibratz. The symmetry and models were D_{2h}:$Fe_2S_2S'_4$, C_{2h}:$Fe_2S_2(SCC)_4$ and C_1:$Fe_2S_2(Cys)_4$. The force constant treatment allowed for the development of a CHARMM-based force field that could be used for all-atom molecular dynamics simulations [74]. The vibrational analysis from all-atom molecular dynamics simulations performed using the CHARMM force field can properly account for the low-energy region of the NRVS spectrum. Extremely low energies involve completely delocalized protein skeleton motion and in-phase motion of the entire [2Fe2S] cluster moving as a rigid body. The precedent set by combining NRVS and molecular dynamics has been further developed with respect to more complex heteroclusters like the iron–molybdenum cofactor in nitrogenase [75].

9.6.4 [4Fe4S] ferredoxin

The ferredoxin of the hyperthermophillic archaeon *Pyrococcus furiosus* contains a [4Fe4S] cluster used for electron transfer. The cluster contains four bridging sulfurs (S^b) that are coordinated to the protein through three cysteinyl sulfurs and a single aspartate oxygen. The D14C mutant (PfD14C Fd) has a point mutation that ensures the [4Fe4S] cluster is coordinated to the protein by four cysteinyl sulfurs (S^t) instead of an aspartate oxygen [76]. The oxidized PfD14C Fd $[4Fe4S]^{2+}$ cluster has been shown in a crystal structure to be highly symmetric with nearly D_{2d} symmetry [77]. In the oxidized $[4Fe4S]^{1+}$ form, the four irons have a formal oxidation of 2.5 and the cluster is S=0. Upon reduction, two irons remain Fe(2.5), two irons become formally ferric, and the cluster becomes S=1/2.

The two oxidation states share three broadly defined vibrational regions (Figure 9.17). The intensity below 100 cm^{-1} arises from the diffuse vibrational modes coupled to protein motion as discussed previously. The region from 100 cm^{-1} to 200 cm^{-1} arises from Fe–S bending-type motion. Finally, the region from 200 cm^{-1} to slightly greater than 400 cm^{-1} involves predominantly Fe–S stretching vibrations; however, this region also has a mixture of Fe–S^t and Fe–S^b stretching vibrations at higher and lower energies, respectively. The oxidized PfD14C Fd NRVS spectrum has the most prominent feature at 148 cm^{-1} with a clear shoulder. There is also a local maximum at 84 cm^{-1}. In the canonically Fe–S stretch region, there are two prominent peaks at 354 cm^{-1} and 382 cm^{-1}. The nearly symmetric A_1 mode at 336 cm^{-1} is very weakly observed in the oxidized NRVS spectrum as it involves very little Fe motion and only S^b "breathing"-type stretch motion. In the cluster bending region, an envelope centered at 281 cm^{-1} is observed.

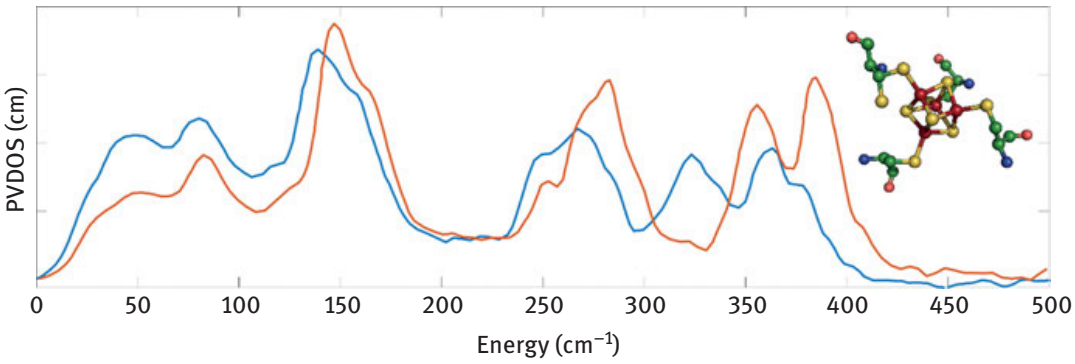

Figure 9.17: NRVS spectrum for [4Fe4S] D14C Ferredoxin in the reduced (——) and oxidized (——) form reproduced from previous work [76]. Inset is the local coordination sphere of the 4Fe4S site.

Although there are many analogies between the oxidized PfD14C Fd NRVS spectrum and existing Raman data, no such comparisons can be drawn for the reduced form as ferredoxins are notoriously difficult to probe with Raman due to fluorescence. Here, NRVS has an obvious advantage over Raman spectroscopy. After reduction, the NRVS spectrum of PfD14C Fd shows a shift of the 382cm^{-1} peak to 362 cm^{-1}, the 354 cm^{-1}, intensity shifts to 320 cm^{-1} and the middle band at 281 cm^{-1} moves to 268.5 cm^{-1}. It is notable that the low-energy region in either oxidation state, which we have defined as involving diffuse phonon-like motion in the protein, is not as dominant as it was in the [2Fe2S] and rubredoxin case.

A combined DFT, force field and molecular dynamics approach to the NRVS spectra indicates that the [4Fe4S] cluster is vibrationally isolated from the rest of the protein. Typically, the coupling between Fe–S motion and S–C–C bends of the cysteine side chains is dependent on the Fe–S–C–C dihedral angle, with a maximum coupling when all four atoms are coplanar at 0 or 180 degrees [78]. The angles in PfD14C Fd are nearer to 90 degrees. Likewise, in the case of the [4Fe4S] cluster each iron is coordinated to the protein matrix by a single sulfur, whereas in the non-Rieske [2Fe2S] and rubredoxin the irons are coordinated to the protein by two and four sulfur bonds per iron, respectively. This has implications for electron transfer – in that protein dynamics in the PfD14C Fd are largely unaffected by the redox of the cluster. In the framework of Marcus theory for electron transfer [79], the reorganization energy term is lower in PfD14C Fd when compared to non-Rieske [2Fe2S] clusters or rubredoxin.

These results help shed some light on questions about biological preferences for which type of FeS cluster is used for electron transfer [80]. Compared to [4Fe4S] clusters, [2Fe2S] clusters may act over shorter distances and/or with long range conformational changes that decouple the electron transfer protein from its redox partner. As in the case of putidaredoxin, which has a 100-fold decrease in binding affinity for its redox partner, cytochrome p450cam, after reduction of its [2Fe2S] [81].

9.6.5 Fe-containing Enzymes

^{57}Fe NRVS has been extended beyond electron-transfer proteins to enzymes with rich chemistry. In Table 9.3 we provide an extensive (but not comprehensive) list of biological NRVS work with a succinct noted observation and, in most cases, list frequencies of interesting ^{57}Fe-X modes. We note that the observations we identify do not fully convey the magnitude of each work and we encourage readers to use them as a guide to read the corresponding full references.

Table 9.3: List of biological NRVS work.

Biological System	Noted Observation	Ref.
Myoglobin Compound-II	Verification of the unprotonated Fe(IV)=O moiety with stretching mode at 805 cm^{-1}.	[82]
Myoglobin-NO	Observation of a ^{15}N-sensitive mode at 547 cm^{-1} assigned as a Fe-NO stretching mode.	[83]
Myoglobin-O_2	Assignment of Fe-O_2 stretching mode at 579 cm^{-1}.	[84]
	Fe-O_2 modes with alternatively substituted porphyrins.	[85]
Myoglobin-CO	Identified heme vibrational dynamics, including delocalization of the heme “doming” mode. Myoglobin-CO stretch at 502cm^{-1} and bend at 572 cm^{-1}.	[86]
[NiFe]-hydrogenase	Identification of the Ni-H-Fe bridging moiety with a wagging mode at 675 cm^{-1}.	[87]
	Assignment of Fe-CO vibrational region between 540–605 cm^{-1} and Fe-CN region between 450–505 cm^{-1}.	[88]
Oxygen-Tolerant [NiFe] hydrogenase	Quantitative determination of the Fe-S cluster composition, specifically identified a [2Fe2S] cluster with a stretching mode at 414 cm^{-1}.	[89]
[FeFe]-hydrogenase	First site-selective ^{57}Fe enrichment for NRVS that demonstrated the $[2Fe]_H$ cluster and $[4Fe4S]_H$ subcluster are inserted stepwise into the protein. [FeFe] site Fe-CO modes: 528, 560, 585, and 604 cm^{-1}. Fe-CN modes: 424 and 454 cm^{-1}.	[90]
	Replacement of the azadithiolate bridge of the [2Fe] site with a proton-disrupting oxodithiolate bridge allows trapping of an intermediate called H_{hyd} with Fe-H-Fe bending modes at 727 and 670 cm^{-1}.	[91]
	Vibrational characterization of the H_{hyd} intermediate, in the enzyme with an artificial azadithiolate $[2^{57}Fe]_H$ cluster. Fe-H-Fe bending modes at 744 (747) and 675 (675)cm^{-1} in CrHydA1(DdHydAB).	[92]
	Characterization of H_{hyd} in the C169S mutant (*Cr*HydA1), altering the proton transfer pathway shifting the Fe-H-Fe bending modes to 772 and 673 cm^{-1}.	[93]
	Characterization of catalytic and oxygen species in the wildtype and C169A mutant (*Cr*HydA1).	[94]
Nitrogenase Fe Protein [4Fe4S] Cluster	First NRVS comparison of a $[4Fe4S]^{2+/1+/0}$ cluster in three oxidation states identifying a linear correlation between oxidation and Fe-S stretching force constants.	[95]

Table 9.3 (continued)

Biological System	Noted Observation	Ref.
Nitrogenase P-cluster Nitrogenase M-cluster Isolated FeMo-co	NRVS spectra of the M-cluster (called "FeMo-co") [7Fe9SMo] deficient enzyme and holoenzyme allowed subtraction of the P-cluster [8Fe7S] and development of an empirical forcefield for the FeMo-co.	[96]
Nitrogenase-CO	Monitored loss of symmetry of the FeMo-co upon binding of CO through a 188 cm^{-1} "breathing mode" of the cofactor.	[97]
Benzoate 1,2-dioxygenase	Assignment of the structure of a peroxide shunt intermediate BZDOp as high-spin side-on Fe(III)-hydroperoxy species. Fe-O stretch identified at 510 cm^{-1}.	[98]
WhiD NsrR	Identification of [4Fe4S]-NO species in NO-sensing regulatory proteins.	[99]
R2lox	Characterization of an O_2 activated species in Fe/Mn and Fe/Fe R2lox indicating a terminal water bound to the Fe/Mn atom and a metal-bridging hydroxide.	[100]

9.7 Outlook

As demonstrated here, the power of NRVS is derived directly from isotopic specificity, normal mode selection and relative sensitivity. Fe is ubiquitous in biological metallocofactors either as part of electron transfer or catalytic mechanisms. Studying these cofactors with traditional vibrational spectroscopy, such as infrared (IR) or Raman spectroscopy, can be impeded by the background created by the biomolecule proper or even fluorescence of the cofactor. As such, the extreme specificity of ^{57}Fe NRVS for only ^{57}Fe motion makes the perfect tool to study vibrational dynamics of the critical Fe-containing components of the biomolecule. Without contributions from the biological sample background, NRVS enjoys very little spectroscopic noise; even modes of Fe hydrides within enzymes [21, 101] have been observed – which are typically difficult to directly identify with other techniques [102, 103]. The selection rules – or comparatively lack thereof – allows for ^{57}Fe NRVS to show both IR- and Raman-active modes that contain ^{57}Fe motion – thus providing a complete picture for Fe vibration.

Since its inception more than two decades ago, ongoing improvements in synchrotron brightness and monochromator resolution have allowed for the investigation of weaker features and more dilute biological samples. Refinement in sample preparations have allowed for high-concentration biological samples and site-of-interest-specific labeling [56]. The technique is continuing to mature, and it is solving questions where resonance Raman and IR spectroscopies cannot. The development

of X-ray free electron lasers of very high flux and monochromation expands the possibilities of NRVS experiments to lower sample concentrations or coupled experiments involving pump lasers or electrochemistry.

References

[1] Mössbauer, R. Kernresonanzfluoreszenz von gammastrahlung in Ir191. Zeitschrift für Physik 1958, 151(2), 124–143.

[2] Mössbauer, R. Kernresonanzabsorption von gammastrahlung in Ir191. Naturwissenschaften 1958, 45(22), 538–539.

[3] Mössbauer Rudolf, L. Kernresonanzabsorption von γ-Strahlung in Ir191. In Zeitschrift für Naturforschung A 1959, 14(p), 211.

[4] Visscher, W. M. Study of lattice vibrations by resonance absorption of nuclear gamma rays. Annals of Physics 1960, 9(2), 194–210.

[5] Singwi, K. S., and Sjölander, A. Diffusive motions in water and cold neutron scattering. Physical Review 1960, 119(3), 863–871.

[6] Sturhahn, W. Nuclear resonant spectroscopy. J Phys Cond Matt 2004, 16, S497–S530.

[7] Lipkin, H. J. Mössbauer sum rules for use with synchrotron sources. Phys Rev B 1995, 52(14), 10073–10079.

[8] Weiss, H., and Langhoff, H. Observation of one phonon transitions in terbium by nuclear resonance fluorescence. Physics Letters A 1979, 69(6), 448–450.

[9] Weiss, H., and Langhoff, H. Observation of localized modes in TbO x using the Mößbauer effect. Zeitschrift für Physik B Condensed Matter 1979, 33(4), 365–368.

[10] Guo, Y. S., Wang, H. X., Xiao, Y. M., Vogt, S., Thauer, R. K., Shima, S., Volkers, P. I., Rauchfuss, T. B., Pelmenschikov, V., Case, D. A., Alp, E. E., Sturhahn, W., Yoda, Y., and Cramer, S. P. Characterization of the Fe site in iron-sulfur cluster-free hydrogenase (Hmd) and of a model compound via nuclear resonance vibrational spectroscopy (NRVS). Inorganic Chemistry 2008, 47(10), 3969–3977.

[11] Mössbauer, R. Kernresonanzabsorption von γ-strahlung in Ir191. In Zeitschrift für Naturforschung A 1959, 14(p), 211.

[12] Singwi, K. S., and Sjölander, A. Resonance absorption of nuclear gamma rays and the dynamics of atomic motions. Physical Review 1960, 120(4), 1093–1102.

[13] RUBY, S., L. Mössbauer experiments without conventional sources. J Phys Colloques 1974, 35 (C6), C6-209-C6-211.

[14] Gerdau, E., Ruffer, R., Winkler, H., Tolksdorf, W., Klages, C. P., and Hannon, J. P. Nuclear bragg-diffraction of synchrotron radiation in yttrium iron-garnet. Physical Review Letters 1985, 54(8), 835–838.

[15] Seto, M., Yoda, Y., Kikuta, S., Zhang, X., and Ando, M. Observation of nuclear resonant scattering accompanied by phonon excitation using synchrotron radiation. Physical Review Letters 1995, 74(19), 3828–3831.

[16] Sturhahn, W., Toellner, T., Alp, E., Zhang, X., Ando, M., Yoda, Y., Kikuta, S., Seto, M., Kimball, C., and Dabrowski, B. Phonon density of states measured by inelastic nuclear resonant scattering. Physical Review Letters 1995, 74(19), 3832–3835.

[17] Chumakov, A. I., Rüffer, R., Grünsteudel, H., Grünsteudel, H. F., Grübel, G., Metge, J., Leupold, O., and Goodwin, H. A. Energy dependence of nuclear recoil measured with incoherent nuclear scattering of synchrotron radiation. EPL (Europhysics Letters) 1995, 30(7), 427.

[18] Achterhold, K., Keppler, C., van Bürck, U., Potzel, W., Schindelmann, P., Knapp, E.-W., Melchers, B., Chumakov, A. I., Baron, A. Q. R., Rüffer, R., and Parak, F. Temperature dependent inelastic X-ray scattering of synchrotron radiation on myoglobin analyzed by the Mössbauer effect. European Biophysics Journal 1996, 25(1), 43–46.

[19] Keppler, C., Achterhold, K., Ostermann, A., van Bürck, U., Potzel, W., Chumakov, A. I., Baron, A. Q. R., Rüffer, R., and Parak, F. Determination of the phonon spectrum of iron in myoglobin using inelastic X-ray scattering of synchrotron radiation. European Biophysics Journal 1997, 25(3), 221–224.

[20] Kamali, S., Wang, H., Mitra, D., Ogata, H., Lubitz, W., Manor, B. C., Rauchfuss, T. B., Byrne, D., Bonnefoy, V., Jenney, F. E. Jr., Adams, M. W., Yoda, Y., Alp, E., Zhao, J., and Cramer, S. P. Observation of the Fe-CN and Fe-CO vibrations in the active site of [NiFe] hydrogenase by nuclear resonance vibrational spectroscopy. Angew Chem Int Ed Engl 2013, 52(2), 724–8.

[21] Ogata, H., Kramer, T., Wang, H., Schilter, D., Pelmenschikov, V., van Gastel, M., Neese, F., Rauchfuss, T. B., Gee, L. B., Scott, A. D., Yoda, Y., Tanaka, Y., Lubitz, W., and Cramer, S. P. Hydride bridge in [NiFe]-hydrogenase observed by nuclear resonance vibrational spectroscopy. Nat Commun 2015, 6, 7890.

[22] Lauterbach, L., Wang, H., Horch, M., Gee, L. B., Yoda, Y., Tanaka, Y., Zebger, I., Lenz, O., and Cramer, S. P. Nuclear resonance vibrational spectroscopy reveals the FeS cluster composition and active site vibrational properties of an O2-tolerant NAD(+)-reducing [NiFe] hydrogenase. Chem Sci 2015, 6(2), 1055–1060.

[23] Kuchenreuther, J. M., Guo, Y. S., Wang, H. X., Myers, W. K., George, S. J., Boyke, C. A., Yoda, Y., Alp, E. E., Zhao, J. Y., Britt, R. D., Swartz, J. R., and Cramer, S. P. Nuclear resonance vibrational spectroscopy and electron paramagnetic resonance spectroscopy of Fe-57-enriched [FeFe] hydrogenase indicate stepwise assembly of the H-cluster. Biochemistry 2013, 52(5), 818–826.

[24] Gilbert-Wilson, R., Siebel, J. F., Adamska-Venkatesh, A., Pham, C. C., Reijerse, E., Wang, H., Cramer, S. P., Lubitz, W., and Rauchfuss, T. B. Spectroscopic investigations of [FeFe] hydrogenase maturated with [57Fe2(adt)(CN)2(CO)4]2–. Journal of the American Chemical Society 2015, 137(28), 8998–9005.

[25] Mitra, D., George, S. J., Guo, Y. S., Kamali, S., Keable, S., Peters, J. W., Pelmenschikov, V., Case, D. A., and Cramer, S. P. Characterization of [4Fe-4S] cluster vibrations and structure in nitrogenase Fe protein at three oxidation levels via combined NRVS, EXAFS, and DFT analyses. Journal of the American Chemical Society 2013, 135(7), 2530–2543.

[26] George, S. J., Barney, B. M., Mitra, D., Igarashi, R. Y., Guo, Y. S., Dean, D. R., Cramer, S. P., and Seefeldt, L. C. EXAFS and NRVS reveal a conformational distortion of the FeMo-cofactor in the MoFe nitrogenase propargyl alcohol complex. Journal of Inorganic Biochemistry 2012, 112, 85–92.

[27] Scott, A., Pelmenschikov, V., Guo, Y., Wang, H., Yan, L., George, S., Dapper, C., Newton, W., Yoda, Y., Tanaka, Y., and Cramer, S. P. J Am Chem Soc 2014, 136, 15942.

[28] Xiao, Y., Smith, M. C., Newton, W., Case, D. A., George, S., Wang, H., Sturhahn, W., Alp, E., Zhao, J., Yoda, Y., and Cramer, S. How nitrogenase shakes – initial information about P-cluster and FeMo-cofactor normal modes from nuclear resonance vibrational spectroscopy (NRVS). Journal of the American Chemical Society 2006, 128(23), 7608–7612.

[29] Leu, B. M., Ching, T. H., Zhao, J. Y., Sturhahn, W., Alp, E. E., and Sage, J. T. Vibrational dynamics of iron in cytochrome c. Journal of Physical Chemistry B 2009, 113(7), 2193–2200.

[30] Sage, J., Durbin, S., Sturhahn, W., Wharton, D., Champion, P., Hession, P., Sutter, J., and Alp, E. Long-range reactive dynamics in myoglobin. Physical Review Letters 2001, 86(21), 4966–4969.

[31] Wong, S. D., Srnec, M., Matthews, M. L., Liu, L. V., Kwak, Y., Park, K., Bell, C. B., 3rd., Alp, E. E., Zhao, J., Yoda, Y., Kitao, S., Seto, M., Krebs, C., Bollinger, J. M. Jr., and Solomon, E. I. Elucidation of the Fe(IV)=O intermediate in the catalytic cycle of the halogenase SyrB2. Nature 2013, 499(7458), 320–3.

[32] Sutherlin, K. D., Liu, L. V., Lee, Y.-M., Kwak, Y., Yoda, Y., Saito, M., Kurokuzu, M., Kobayashi, Y., Seto, M., Que, L., Nam, W., and Solomon, E. I. Nuclear resonance vibrational spectroscopic definition of peroxy intermediates in nonheme iron sites. Journal of the American Chemical Society 2016, 138(43), 14294–14302.

[33] Serrano, P. N., Wang, H., Crack, J. C., Prior, C., Hutchings, M. I., Thomson, A. J., Kamali, S., Yoda, Y., Zhao, J., Hu, M. Y., Alp, E. E., Oganesyan, V. S., Le Brun, N. E., and Cramer, S. P. Nitrosylation of nitric-oxide-sensing regulatory proteins containing [4Fe-4S] clusters gives rise to multiple iron–nitrosyl complexes. Angewandte Chemie International Edition 2016, 55(47), 14575–14579.

[34] Sturhahn, W., CONUSS and PHOENIX: evaluation of nuclear resonant scattering data. 2000, 125, 149–172.

[35] Brown, D. E., Toellner, T. S., Sturhahn, W., Alp, E. E., Hu, M., Kruk, R., Rogacki, K., and Canfield, P. C. Partial phonon density of states of dysprosium and its compounds measured using inelastic nuclear resonance scattering. Hyperfine Interactions 2004, 153(1), 17–24.

[36] Ishikawa, D., Baron, A. Q. R., and Ishikawa, T. Nuclear resonant scattering from the subnanosecond lifetime excited state of ^{201}Hg. Phys Rev B 2005, 72, 140301(R.

[37] Barla, A., Rüffer, R., Chumakov, A. I., Metge, J., Plessel, J., and Abd-Elmeguid, M. M. Direct determination of the phonon density of states in beta-Sn. Phys Rev B 2000, 61(22), R14881–R14884.

[38] Giefers, H., Tanis, E. A., Rudin, S. P., Greeff, C., Ke, X., Chen, C., Nicol, M. F., Pravica, M., Pravica, W., Zhao, J., Alatas, A., Lerche, M., Sturhahn, W., and Alp, E. Phonon density of states of metallic Sn at high pressure. Phys Rev Lett 2007, 98, 245502.

[39] Toellner, T. S., Hu, M. Y., Sturhahn, W., Quast, K., and Alp, E. E. Inelastic nuclear resonant scattering with sub-meV energy resolution. Applied Physics Letters 1997, 71(15), 2112–2114.

[40] Sage, J. T., Paxson, C., Wyllie, G. R. A., Sturhahn, W., Durbin, S. M., Champion, P. M., Alp, E. E., and Scheidt, W. R. Nuclear resonance vibrational spectroscopy of a protein active-site mimic. J Phys Condens Matter 2001, 13, 7707–7722.

[41] Leu, B. M., Zgierski, M. Z., Wyllie, G. R. A., Ellison, Mary K., Scheidt, W. R., Sturhahn, W., Alp, E. E., Durbin, S. M., and Sage, J. T. Vibrational dynamics of biological molecules: multi-quantum contributions. J Phys Chem Solids 2005, 66, 2250–2256.

[42] Pavlik, J. W., Barabanschikov, A., Oliver, A. G., Alp, E. E., Sturhahn, W., Zhao, J., Sage, J. T., and Scheidt, W. R., Probing vibrational anisotropy with nuclear resonance vibrational spectroscopy. 2010, 49, 4400 –4404.

[43] Hu, M. Y., Sturhahn, W., Toellner, T. S., Mannheim, P. D., Brown, D. E., Zhao, J. Y., and Alp, E. E. Measuring velocity of sound with nuclear resonant inelastic x-ray scattering. Phys Rev B 2003, 67(9), 094304.

[44] Lipkin, H. J. Mössbauer sum rules for use with synchrotron sources. Hyperfine Interactions 1999, 123(1), 349–366.

[45] Toellner, T. S. Monochromatization of synchrotron radiation for nuclear resonant scattering experiments. Hyperfine Interactions 2000, 125(1), 3–28.

[46] The European synchrotron facility. http://www.esrf.eu/home/UsersAndScience/Accelerators/parameters.html.

[47] ESRF – high resolution monochromator. http://www.esrf.eu/home/UsersAndScience/Experiments/MEx/ID18/beamline_layout/optics/HRM.html (accessed 11/6/2017).

[48] Insertion devices by sector | advanced photon source. https://www1.aps.anl.gov/Magnetic-Devices/Insertion-Devices/Insertion-Devices-by-Sector.
[49] Beamlines information | advanced photon source. https://www1.aps.anl.gov/Beamlines/Directory/Details?beamline_id=6.
[50] SPring-8 – Introduction to insertion devices. http://www.spring8.or.jp/en/about_us/whats_sp8/facilities/bl/light_source_optics/sources/insertion_device/intro_insertion_devices (accessed 11/6/2017).
[51] Yoshitaka, Y., Kyoko, O., Hongxin, W., Stephen, P. C., and Makoto, S. High-resolution monochromator for iron nuclear resonance vibrational spectroscopy of biological samples. Japanese Journal of Applied Physics 2016, 55(12), 122401.
[52] Wang, H., Yoda, Y., Kamali, S., Zhou, Z. H., and Cramer, S. P. Real sample temperature: a critical issue in the experiments of nuclear resonant vibrational spectroscopy on biological samples. Journal of synchrotron radiation 2012, 19(Pt 2), 257–63.
[53] Wang, H., Yoda, Y., Ogata, H., Tanaka, Y., and Lubitz, W. A strenuous experimental journey searching for spectroscopic evidence of a bridging nickel-iron-hydride in [NiFe] hydrogenase. Journal of Synchrotron Radiation 2015, 22(6), 1334–1344.
[54] PetraIII – P01 – unified data sheet. http://photon-science.desy.de/facilities/petra_iii/beamlines/p01_dynamics/unified_data_sheet_p01/index_eng.html (accessed 11/6/2017).
[55] PetraIII – P01 – high resolution monochromators. http://photon-science.desy.de/facilities/petra_iii/beamlines/p01_dynamics/nuclear_resonant_scattering_station/high_resolution_monochromators/index_eng.html (accessed 11/6/2017).
[56] Reijerse, E. J., Pham, C. C., Pelmenschikov, V., Gilbert-Wilson, R., Adamska-Venkatesh, A., Siebel, J. F., Gee, L. B., Yoda, Y., Tamasaku, K., Lubitz, W., Rauchfuss, T. B., and Cramer, S. P. Direct observation of an iron-bound terminal hydride in [FeFe]-hydrogenase by nuclear resonance vibrational spectroscopy. J Am Chem Soc 2017, 139(12), 4306–4309.
[57] Kohn, V. G., and Chumakov, A. I. DOS: Evaluation of phonon density of states from nuclear resonant inelastic absorption. Hyperfine Interactions 2000, 125(1–4), 205–221.
[58] Sturhahn, W. CONUSS and PHOENIX: evaluation of nuclear resonant scattering data. Hyp Interac 2000, 125, 149–172.
[59] Johnson, D. W., and Spence, J. C. H. Determination of the single-scattering probability distribution from plural-scattering data. Journal of Physics D Applied 1974, 771.
[60] Zhao, J. Y., and Sturhahn, W. High-energy-resolution X-ray monochromator calibration using the detailed-balance principle. Journal of Synchrotron Radiation 2012, 19, 602–608.
[61] Dowty, E. Fully automated microcomputer calculation of vibrational spectra. Physics and Chemistry of Minerals 1987, 14(1), 67–79.
[62] Petrenko, T., Sturhahn, W., and Neese, F. First-principles calculation of nuclear resonance vibrational spectra. Hyperfine Interactions 2008, 175(1–3), 165–174.
[63] Do, L. H., Wang, H., Tinberg, C. E., Dowty, E., Yoda, Y., Cramer, S. P., and Lippard, S. J. Characterization of a synthetic peroxodiiron(III) protein model complex by nuclear resonance vibrational spectroscopy. Chemical communications (Cambridge, England) 2011, 47(39), 10945–7.
[64] Do, L. H., Hayashi, T., Moënne-Loccoz, P., and Lippard, S. J. Carboxylate as the protonation site in (Peroxo)diiron(III) model complexes of soluble methane monooxygenase and related diiron proteins. Journal of the American Chemical Society 2010, 132(4), 1273–1275.
[65] Dong, Y., Menage, S., Brennan, B. A., Elgren, T. E., Jang, H. G., Pearce, L. L., and Que, L. Dioxygen binding to diferrous centers. models for diiron-oxo proteins. Journal of the American Chemical Society 1993, 115(5), 1851–1859.
[66] Park, K., Tsugawa, T., Furutachi, H., Kwak, Y., Liu, L. V., Wong, S. D., Yoda, Y., Kobayashi, Y., Saito, M., Kurokuzu, M., Seto, M., Suzuki, M., and Solomon, E. I. Nuclear resonance

vibrational spectroscopy and DFT study of peroxo-bridged biferric complexes: structural insight into peroxo intermediates of binuclear non-heme iron enzymes. Angew Chem Int Ed Engl 2013, 52(4), 1294–8.

[67] Park, K., Li, N., Kwak, Y., Srnec, M., Bell, C. B., Liu, L. V., Wong, S. D., Yoda, Y., Kitao, S., Seto, M., Hu, M., Zhao, J., Krebs, C., Bollinger, J. M., and Solomon, E. I. Peroxide activation for electrophilic reactivity by the binuclear non-heme iron enzyme aurF. Journal of the American Chemical Society 2017, 139(20), 7062–7070.

[68] Xiao, Y., Wang, H., George, S. J., Smith, M. C., Adams, M. W., Jenney, F. E. Jr., Sturhahn, W., Alp, E. E., Zhao, J., Yoda, Y., Dey, A., Solomon, E. I., and Cramer, S. P. Normal mode analysis of Pyrococcus furiosus rubredoxin via nuclear resonance vibrational spectroscopy (NRVS) and resonance Raman spectroscopy. J Am Chem Soc 2005, 127(42), 14596–606.

[69] Day, M. W., Hsu, B. T., Joshua-Tor, L., Park, J. B., Zhou, Z. H., Adams, M. W., and Rees, D. C. X-ray crystal structures of the oxidized and reduced forms of the rubredoxin from the marine hyperthermophilic archaebacterium Pyrococcus furiosus. Protein Sci 1992, 1(11), 1494–507.

[70] Bau, R., Rees, D. C., Kurtz Jr., D. M., Scott, R. A., Huang, H., Adams, M. W. W., and Eidsness, M. K. Crystal structure of rubredoxin from Pyrococcus furiosus at 0.95 Å resolution, and the structures of N-terminal methionine and formylmethionine variants of Pf Rd. contributions of N-terminal interactions to thermostability. JBIC Journal of Biological Inorganic Chemistry 1998, 3(5), 484–493.

[71] Guo, Y., Brecht, E., Aznavour, K., Nix, J. C., Xiao, Y., Wang, H., George, S. J., Bau, R., Keable, S., Peters, J. W., Adams, M. W. W., Jenney, F. E., Sturhahn, W., Alp, E. E., Zhao, J., Yoda, Y., and Cramer, S. P. Nuclear resonance vibrational spectroscopy (NRVS) of rubredoxin and MoFe protein crystals. Hyperfine Interactions 2012, 222(S2), 77–90.

[72] Xiao, Y., Tan, M. L., Ichiye, T., Wang, H., Guo, Y., Smith, M. C., Meyer, J., Sturhahn, W., Alp, E. E., Zhao, J., Yoda, Y., and Cramer, S. P. Dynamics of rhodobacter capsulatus [2FE-2S] ferredoxin VI and aquifex aeolicus ferredoxin 5 via nuclear resonance vibrational spectroscopy (NRVS) and resonance Raman spectroscopy. Biochemistry 2008, 47(25), 6612–27.

[73] Fu, W., Drozdzewski, P. M., Davies, M. D., Sligar, S. G., and Johnson, M. K. Resonance Raman and magnetic circular dichroism studies of reduced [2Fe-2S] proteins. J Biol Chem 1992, 267 (22), 15502–10.

[74] Brooks, B. R., Brooks, C. L. 3rd, Mackerell, A. D. Jr., Nilsson, L., Petrella, R. J., Roux, B., Won, Y., Archontis, G., Bartels, C., Boresch, S., Caflisch, A., Caves, L., Cui, Q., Dinner, A. R., Feig, M., Fischer, S., Gao, J., Hodoscek, M., Im, W., Kuczera, K., Lazaridis, T., Ma, J., Ovchinnikov, V., Paci, E., Pastor, R. W., Post, C. B., Pu, J. Z., Schaefer, M., Tidor, B., Venable, R. M., Woodcock, H. L., Wu, X., Yang, W., York, D. M., and Karplus, M. CHARMM: the biomolecular simulation program. J Comput Chem 2009, 30(10), 1545–614.

[75] Gee, L. B., Leontyev, I., Stuchebrukhov, A., Scott, A. D., Pelmenschikov, V., and Cramer, S. P. Docking and migration of carbon monoxide in nitrogenase: the case for gated pockets from infrared spectroscopy and molecular dynamics. Biochemistry 2015, 54(21), 3314–9.

[76] Mitra, D., Pelmenschikov, V., Guo, Y., Case, D. A., Wang, H., Dong, W., Tan, M.-L., Ichiye, T., Jenney, F. E., Adams, M. W. W., Yoda, Y., Zhao, J., and Cramer, S. P. Dynamics of the [4Fe-4S] cluster in Pyrococcus furiosus D14C ferredoxin via nuclear resonance vibrational and resonance Raman spectroscopies, force field simulations, and density functional theory calculations. Biochemistry 2011, 50(23), 5220–35.

[77] Lovgreen, M. N., Martic, M., Windahl, M. S., Christensen, H. E., and Harris, P. Crystal structures of the all-cysteinyl-coordinated D14C variant of Pyrococcus furiosus ferredoxin: [4Fe-4S] <–> [3Fe-4S] cluster conversion. J Biol Inorg Chem 2011, 16(5), 763–75.

[78] Czernuszewicz, R. S., Kilpatrick, L. K., Koch, S. A., and Spiro, T. G. Resonance Raman spectroscopy of Iron(III) tetrathiolate complexes: implications for the conformation and force field of rubredoxin. Journal of the American Chemical Society 1994, 116(16), 7134–7141.
[79] Marcus, R. A. On the theory of oxidation—reduction reactions involving electron transfer. V. Comparison and properties of electrochemical and chemical rate constants1. The Journal of Physical Chemistry 1963, 67(4), 853–857.
[80] Meyer, J. Iron–sulfur protein folds, iron–sulfur chemistry, and evolution. JBIC Journal of Biological Inorganic Chemistry 2008, 13(2), 157–170.
[81] Pochapsky, T. C., Kostic, M., Jain, N., and Pejchal, R. Redox-dependent conformational selection in a Cys4Fe2S2 ferredoxin. Biochemistry 2001, 40(19), 5602–5614.
[82] Zeng, W., Barabanschikov, A., Zhang, Y., Zhao, J., Sturhahn, W., Alp, E. E., and Sage, J. T. Journal of the American Chemical Society, 2008, 130, 1816–1817.
[83] Zeng, W., Silvernail, N. J., Wharton, D. C., Georgiev, G. Y., Leu, B. M., Scheidt, W. R., Zhao, J., Sturhahn, W., Alp, J. T., and Sage, E. E. Journal of the American Chemical Society, 2005, 127, 11200–11201.
[84] Zeng, W. Q., Barabanschikov, A., Wang, N. Y., Lu, Y., Zhao, J. Y., Sturhahn, W., Alp, E. E., and Sage, J. T., Chemical Communications, 2012, 48, 6340–6342.
[85] Ohta, T., Shibata, T., Kobayashi, Y., Yoda, Y., Ogura, T., Neya, S., Suzuki, A., Seto, M., and Yamamoto, Y., Biochemistry, 2018, 57, 6649–6652.
[86] Sage, J. T., Durbin, S. M., Sturhahn, W., Wharton, D. C., Champion, P. M., Hession, P., Sutter, J., and Alp, E. E., Physical Review Letters, 2001, 86, 4966–4969.
[87] Ogata, H., Kramer, T., Wang, H., Schilter, D., Pelmenschikov, V., van Gastel, M., Neese, F., Rauchfuss, T. B., Gee, L. B., Scott, A. D., Yoda, Y., Tanaka, Y., Lubitz, W., and Cramer, S. P., Nat Commun, 2015, 6, 7890.
[88] Kamali, S., Wang, H., Mitra, D., Ogata, H., Lubitz, W., Manor, B. C., Rauchfuss, T. B., Byrne, D., Bonnefoy, V., Jenney, F. E. Jr., Adams, M. W., Yoda, Y., Alp, E., Zhao, J., and Cramer, S. P., Angew Chem Int Ed Engl, 2013, 52, 724–728.
[89] Lauterbach, L., Wang, H., Horch, M., Gee, L. B., Yoda, Y., Tanaka, Y., Zebger, I., Lenz, O., and Cramer, S. P., Chem Sci, 2015, 6, 1055–1060.
[90] Mitra, D., Pelmenschikov, V., Guo, Y., Case, D. A., Wang, H., Dong, W., Tan, M.-L., Ichiye, T., Jenney, F. E., Adams, M. W. W., Yoda, Y., Zhao, J., and Cramer, S. P., Biochemistry, 2011, 50, 5220–5235.
[91] Reijerse, E. J., Pham, C. C., Pelmenschikov, V., Gilbert-Wilson, R., Adamska-Venkatesh, A., Siebel, J. F., Gee, L. B., Yoda, Y., Tamasaku, K., Lubitz, W., Rauchfuss, T. B., and Cramer, S. P., J Am Chem Soc, 2017, 139, 4306–4309.
[92] Pelmenschikov, V., Birrell, J. A., Pham, C. C., Mishra, N., Wang, H., Sommer, C., Reijerse, E., Richers, C. P., Tamasaku, K., Yoda, Y., Rauchfuss, T. B., Lubitz, W., and Cramer, S. P., J Am Chem Soc, 2017, 139, 16894–16902.
[93] Pham, C. C., Mulder, D. W., Pelmenschikov, V., King, P. W., Ratzloff, M. W., Wang, H., Mishra, N., Alp, E. E., Zhao, J., Hu, M. Y., Tamasaku, K., Yoda, Y., and Cramer, S. P., Angew Chem Int Ed Engl, 2018, 57, 10605–10609.
[94] Mebs, S., Kositzki, R., Duan, J., Kertess, L., Senger, M., Wittkamp, F., Apfel, U.-P., Happe, T., Stripp, S. T., Winkler, M., and Haumann, M., Biochimica et Biophysica Acta (BBA) - Bioenergetics, 2018, 1859, 28–41.
[95] Mitra, D., George, S. J., Guo, Y. S., Kamali, S., Keable, S., Peters, J. W., Pelmenschikov, V., Case, D. A., and Cramer, S. P., Journal of the American Chemical Society, 2013, 135, 2530–2543.

[96] Xiao, Y., Wang, H., George, S. J., Smith, M. C., Adams, M. W., Jenney, F. E., Jr., Sturhahn, W., Alp, E. E., Zhao, J., Yoda, Y., Dey, A., Solomon, E. I., and Cramer, S. P., J Am Chem Soc, 2005, 127, 14596–14606.
[97] Scott, A. D., Pelmenschikov, V., Guo, Y., Yan, L., Wang, H., George, S. J., Dapper, C. H., Newton, W. E., Yoda, Y., Tanaka, Y., and Cramer, S. P., Journal of the American Chemical Society, 2014, 136, 15942–15954.
[98] Sutherlin, K. D., Rivard, B. S., Böttger, L. H., Liu, L. V., Rogers, M. S., Srnec, M., Park, K., Yoda, Y., Kitao, S., Kobayashi, Y., Saito, M., Seto, M., Hu, M., Zhao, J., Lipscomb, J. D., and Solomon, E. I., Journal of the American Chemical Society, 2018, 140, 5544–5559.
[99] Serrano, P. N., Wang, H., Crack, J. C., Prior, C., Hutchings, M. I., Thomson, A. J., Kamali, S., Yoda, Y., Zhao, J., Hu, M. Y., Alp, E. E., Oganesyan, V. S., Le Brun, N. E., and Cramer, S. P., Angewandte Chemie International Edition, 2016, 55, 14575–14579.
[100] Mebs, S., Srinivas, V., Kositzki, R., Griese, J. J., Högbom, M., and Haumann, M., Biochimica et Biophysica Acta (BBA) - Bioenergetics, 2019, 1860, 148060.
[101] Reijerse, E. J., Pelmenschikov, V., Gilbert-Wilson, R., Adamska-Venkatesh, A., Siebela, J.F., Gee, L. B., Yoda, Y., Tamasaku, K., Lubitz, W., Rauchfuss, T. B., and Cramer, S. P. Direct observation of an iron-bound terminal hydride in [FeFe]-hydrogenase by nuclear resonance vibrational spectroscopy. Submitted 2016.
[102] Rosenberg, E. Kinetic deuterium isotope effects in transition metal hydride clusters. Polyhedron 1989, 8(4), 383–405.
[103] Kaesz, H. D., and Saillant, R. B. Hydride complexes of the transition metals. Chemical Reviews 1972, 72(3), 231–281.